Ground surface classification by stereo polarised image sensors

Master's thesis in Computer science and engineering

Jan Jürgen Eisenmenger

Ground surface classification by stereo polarised image sensors

Jan Jürgen Eisenmenger

UNIVERSITY OF
GOTHENBURG

CHALMERS
UNIVERSITY OF TECHNOLOGY

Ground surface classification by stereo polarised image sensors

Jan Jürgen Eisenmenger

Ground surface classification by stereo polarised image sensors

Jan Jürgen Eisenmenger Department of Computer Science and Engineering
Chalmers University of Technology and University of Gothenburg

Abstract

Detecting where water hazards are on a road is a non-trivial task for a computer or an autonomous vehicle. By introducing polarized imaging, advances in water hazard detection have been made in recent years. However, most approaches utilize retrofitted polarized cameras for use in an off-road environment. In this thesis, a dedicated polarized imaging sensor, the IMX250MZR, is used in order to investigate the feasibility of polarization based water hazard detection in an urban environment. Stereo imaging was used in order to measure the distance to the detected hazards, but failed due to the lack of features on the road surface. Results show that detection works well when the camera is facing away from the sun, with poor results when looking towards the sun, due to the different polarization in the sky.

Acknowledgements

I would like to thank my academic supervisor Ole Martin Christensen and company advisor Thomas Petig for their continuous support and feedback throughout the run of this thesis. A special thanks to Qamcom Research and Technology for providing the cameras and hardware.

Jan Jürgen Eisenmenger, Gothenburg, August 2020

Contents

1

Introduction

The distinction of different road surfaces is a frequent task for a human driver. It is necessary to adjust one's driving style to the conditions, like ice or water. The task of detecting water or ice is especially hard for an autonomous vehicle [NMM17].

One possibility to detect reflective surfaces, such as water, is to rely on their polarizing properties. Polarization refers to the direction in which the electromagnetic wave vibrates. This direction changes, depending on the reflection. Since polarization is not visible to the naked eye, we have to deploy polarized imaging in order to measure it.

One way to achieve this is by placing a polarizing filter in front of a general purpose camera. However, recent advancements in sensor technology resulted in an image sensor, where four differently aligned polarizing filters have been placed on the sensor chip itself, on a per pixel basis. This sensor, the IMX250MZR [Son18], provides dedicated polarizing capabilities, which should result in higher quality imaging compared to the retrofitted counterparts.

An investigation into the capabilities of the IMX250MZR in terms of water detection should provide useful insight in both the sensor and water detection via polarized imaging itself.

1.1   Background

Polarization has been used as a criterion for water detection before. Most of those approaches generally measure polarization by using two or more cameras, each with a differently aligned polarized filter placed in front of the lens.

For example, Bin Xie et al. used three cameras with retrofitted filters in order to measure and calculate the Degree and Angle of Polarization for off-road water hazard detection [Bin+07]. However, they do not take stereo distance measurements into account and focus on an off-road environment. Additionally, their main focus lies on a so called Similarity Degree. This metric appeared to be unusable in an urban environment, which will be shown later in Subsection 3.3.3.

Yang et al. used a head-mounted stereo camera setup, with two retrofitted filters. They rely on the Degree of Polarization for water hazard detection. However, they only detect water right in front of the test subject and therefore with a very high angle of incidence of 70° [Yan+17]. This results in a different polarization on the water hazards compared to a low angle, as will be shown later.

Nguyen, Milford, and Mahony focused on detecting and tracking water hazard in an

3D environment, using two cameras in a stereo setup. They measure polarization by deploying a 0° and 90° polarizing filter in front of either camera. Their focus lies on the influence of the position of the sun on the polarization of the water hazards. However, they use the polarization data to train a Gaussian Mixture Model for the classification of water and non-water, rather than performing image processing based on the polarization values [NMM17].

Shen et al. have also been investigating how the position of the sun influences polarization patterns for imaging processes. They focus on the detection of non-water objects on water and not on a road surface.

Han et al. introduced a new dataset for water hazard detection, using polarized images as the ground truth. Since the work in this thesis relies on the polarization capabilities of the IMX250MZR, this dataset can not be used. The authors also used Artificial Intelligence with a new type of deep network unit in order to detect water hazards reliably [Han+18].

Most of the previous approaches rely on general purpose cameras that have been retrofitted with polarization filters. This makes it so that each camera can only measure the intensity of a single phase, therefore requiring multiple cameras in order to produce a complete overview of the polarization.

The IMX250MZR has, to the knowledge of the author, not been used in the particular setting of water hazard detection. There have been surveys about its performance, i.e. [RRN19]. They focus more on the technical aspects of the sensor however.

There have also been approaches that did not factor in polarization at all. They more closely rely on color and brightness values. For example, Yao, Xiang, and Liu use machine learning and general image segmentation for water detection on general purpose digital cameras. Their algorithm seems to focus more on larger areas of water, like lakes and not smaller puddles on a road however [YXL09]. Additionally, their results suggest that they are only able to detect water when it is directly reflecting the sky.

Zhao et al. rely on the brightness and saturation difference between water reflecting the sky and the surrounding terrain. They also take the low texture of water compared to the surrounding areas into account [Zha+13].

Rankin, Matthies, and Bellutta also introduce water detection based on the same cues. They additionally relate those values to the incidence angle of the camera to the given water surface. The lower the incidence angle, the more the color on the surface is influenced by the reflection. Therefore, this also relies on water completely reflecting the sky [RMB11].

Another approach was given by Shao, Zhang, and Li. They project a horizontal line of light on the ground, at different positions. Depending on how the line is visible on the ground, they can tell where a water hazard is present on the horizontal line, amongst other categories. This process works well even during the day, but requires an appropriate emitter [SZL15].

1.2 Problem Domain and Motivation

Most of the previous approaches have one thing in common: They mainly work in offroad environments, with the use case being an Unmanned Ground Vehicle (UGV). A UGV needs to avoid deep puddles in order to not get stuck, making smaller, wet surfaces not a large problem. In an urban environment, wet surfaces do matter, since they influence the breaking distance for vehicles. This is important for an unmanned vehicle in a traffic situation. Additionally, the ground surface differs from an offroad environment, consisting of a more even and regular surface, thus making the differentiation between water and non-water more difficult and interesting. The urban environment also poses challenges in terms of polarization, since places without direct sunlight are likely differently polarized.

Another aspect are the capabilities of the IMX250MZR. As previously mentioned, most of the previous approaches that rely on polarization have made use of general purpose cameras that have been retrofitted with polarizing filters. Applying a dedicated imaging sensor to the area of water detection via polarization could possibly produce better results than previously had been seen. For this, the actual capabilities and accuracy of the IMX250MZR will need to be investigated.

1.3 Research Goal and Research Questions

This thesis aims to present an investigation into if and how the IMX250MZR can be used for water detection using polarization as a cue, in an urban environment. In order to achieve this, the following questions will be answered.

1. How accurate is the polarization data coming from the IMX250MZR?
2. How much does the position of the sun influence the polarization on the ground?
3. Is it possible to use the IMX250MZR in a stereo setup for distance measurements?
4. Can image processing be used to segment water hazards from the scene by relying on polarization data?
5. What challenges does an urban environment provide?

The final goal is not to provide a system which can reliably detect water hazards and track the distance, but rather show how and if one could use the IMX250MZR in order to do so.

1.4 Limitations

This thesis restricts the detection of water hazards to use straightforwards image processing, rather than relying on probabilistic models or machine learning.

Additionally, all reference images will be taken during clear skies in order to reduce the variety of sky polarization.

Since the goal is investigate the feasibility of a water detection algorithm on the IMX250MZR rather than a high performing system, the final algorithm will not be compared to previous approaches. This is mostly motivated due to the difference in

environment, where an in-depth comparison can not be conducted along the same base and ground truth. This does not only refer to the difference in ground surface, either asphalt or dirt, but also the conditions in the sky. Most previous approaches do not restrict themselves to particular weather conditions, unlike in this thesis.

The difference in camera also plays a role. Since the type of data that is coming from the IMX250MZR and the previous setups with retrofitted filters differs, the approaches are only partially comparable.

1.5   Structure of the Thesis

The thesis is structured as follows. Chapter 2 introduces the theoretical concepts behind polarization and stereo imaging. Chapter 3 describes how those concepts can be implemented based on the format of the IMX250MZR. Additionally, the proposed algorithm for water hazard detection will be outlined as well as the experiments that aided the creation. Chapter 4 evaluates the IMX250MZR based on the polarization calculations that have been established in Chapter 3. Chapter 5 discusses the results as produced by the algorithm as well as how the detection could be improved in the future. Chapter 6 concludes the thesis by summarizing the results.

2
Theory

This chapter will lay the theoretical foundations necessary for understanding how polarized light can be used to detect water. Additionally, an introduction into 3D-imaging via stereoscopic pictures is given.

2.1 Polarization

What we commonly refer to as light is but a small fraction of the whole range of electromagnetic (EM) radiation. The only thing special about the part of the EM-spectrum we call light is that human eyes can perceive it. There is no distinction when it comes to physical properties. We will therefore refer to electromagnetic radiation in general for the following section.

For our intents and purposes we can refer to electromagnetic radiation as oscillations in the electric and magnetic field. They propagate in the form of a *transverse wave*. This means that the electric and magnetic fields oscillate perpendicular to the direction in which the wave spreads, see Figure 2.1 [Gol16].
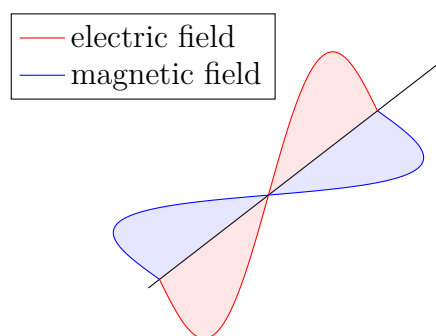
Figure 2.1: Components of a transverse wave. Note that the electric and magnetic field are perpendicular to each other.

For the human eye the relevant factors in sensing light are the wavelength and the amplitude of the wave. The wavelength refers to the colour that is being perceived, the amplitude to the intensity or brightness [Bin+07]. To describe the wave completely more parameters than these two are needed, one of them being polarization.

2.1.1 Types of Polarization

In optics, **Polarization** refers to the direction in which the electric field vibrates [Gol16]. The polarization of a wave is dependent on the direction of the electric field vector [SM07]. The tip of the vector describes the current amplitude of the electric field. The endpoint of the electric field vector describes a particular shape over time which defines the form of polarization for that specific wave [Gol16].

The shape indicated is generally speaking an ellipse, a circle and a line can be seen as special cases, which results in the three forms of polarization: Linear, circular and elliptical [Gol16].

Any single electromagnetic wave is always **linearly polarized**. Although the wave consists of the two transverse components, the electric and magnetic field wave, only the electric wave is relevant for polarization. The endpoint of the electric field vector oscillates in a straight line for a single wave, therefore, the wave is linearly polarized, see Figure 2.2.

$\longrightarrow$ electric field vector
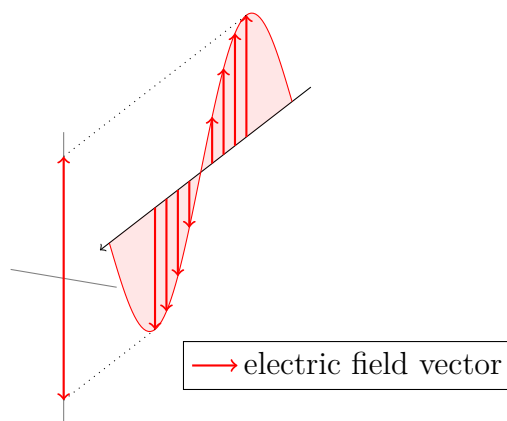
Figure 2.2: Vertically polarized wave.

By combining two different orthogonal waves or using a different reference frame, it is possible to obtain different shapes. Adding the two electric field vectors of each wave results in a new, combined electric field vector, describing the polarization of the two waves as one. The waves have to share the same frequency since they would interfere otherwise [RSC05].

In the simple case of both waves being in the same phase the result electric field vector still oscillates in a linear fashion, see Figure 2.3. The particular angle of the linear polarization is the result of the difference in amplitude between the two component waves. This so called Angle of Polarization (AOP) is the angle between a linearly polarized light wave and a reference plane [Zho+17].
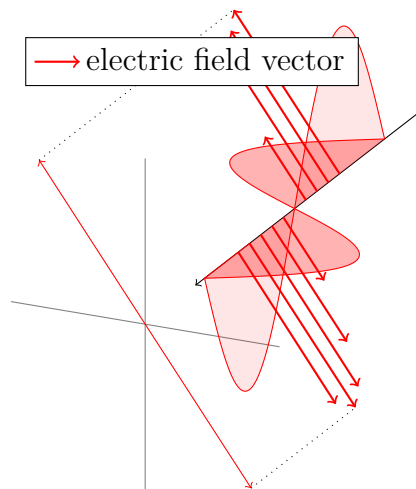
Figure 2.3: Linearly polarized wave, consisting of two transverse components.

If a phase shift is introduced between the two waves, the direction of the electric field vector describes an ellipse, see Figure 2.4.
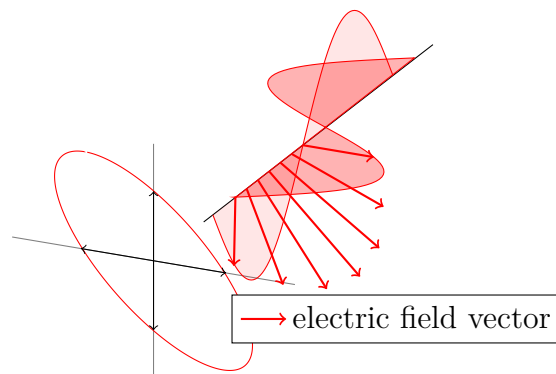
Figure 2.4: Elliptic polarization.

Depending on the size of the offset as well as the amplitudes of the different waves the shape of ellipse changes.

The particular case of identical amplitudes and an offset of 90° ($\frac{\pi}{2}$), is described as circular polarization, see Figure 2.5.

In any case, the direction of the offset influences the handedness of the polarization. As the wave propagates, it can either be left- or right-handed. A wave is right-handed if the tip of the electric field vector describes a clockwise motion, with the beam coming towards the observer [Gol16].
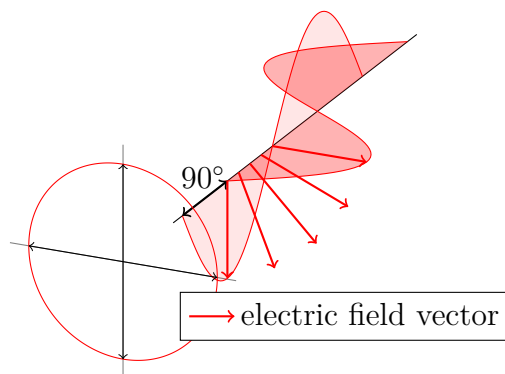
Figure 2.5: Circular polarization.

The existence of polarized light implies **unpolarized light** as well. Unpolarized light is not a form of polarization per se, since a wave will always have an electric field vector and will consequently be polarized. Unpolarized light can only be observed as a superposition of multiple waves, each having their own random direction of polarization. It can also be described as light without a polarization structure. This is generally the case for most natural or human made light sources. The particular electromagnetic radiation features a variety of random phases and also polarizations [LLP96].
From this point on, we will refer to polarized light as a collection of waves that share the same polarization and not just a single wave.

2.1.2 Reflecting Light

Reflection itself can be split into two categories: Diffuse and specular reflection. **Diffuse** reflection can be observed when light is reflected by a rough surface. The light gets scattered in different directions, due to the irregular shape of the material. On the other hand, **specular reflection** occurs when the light is reflected by a smooth surface, like a mirror. The relative shape and angles of the incoming rays are kept intact. For example, if the incoming rays are parallel to each other, the reflected rays will be so as well. While the rest of this section holds true for both types of reflection, we will generally be referring to specular reflection.

The reflection of light has different properties depending on the type or direction of the polarization. In general, it is defined by two values: The angle of incidence and the angle of refraction.
The angle of incidence θ_i is the angle between the incoming ray and the normal vector $\hat{n}$ of the respective reflecting surface, see Figure 2.6. On the other side, the angle of refraction θ_r is the angle between the refracted ray and the inverted normal vector. The ray, as well as the normal vector, lies on the *plane of incidence*. It is defined as the plane which contains the incidence ray [Gol16].
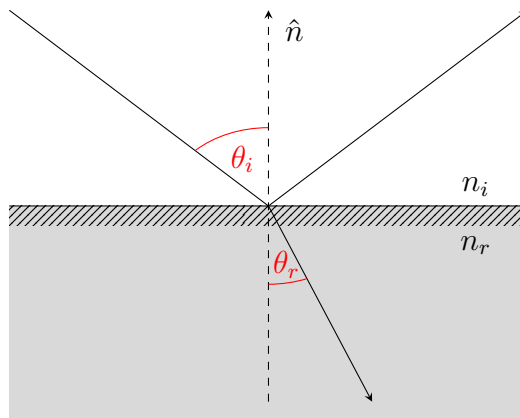
Figure 2.6: Reflection of light with the relevant parameters.

The angle of refraction depends on the angle of incidence, as well as the refractive indices n_i and n_r of the two mediums in question. They describe the speed of light in the particular medium. The difference in speed causes the refraction and can therefore be used to calculate the θ_i or θ_i from each other. SNELL'S LAW describes the relation between the angles and refractive indices as stated in Equation 2.1.

$$n_i sin(\theta_i) = n_r sin(\theta_r) \tag{2.1}$$

Light reflects and refracts differently based on the orientation of the polarization. Considering the plane of incidence, there are two general cases regarding the orientation of the polarization: s- and p-polarization.

In **s-polarization**, the orientation of the polarization is perpendicular to the plane of incidence. It is therefore parallel to the surface as well. Using the Fresnel equations, we can calculate how much of the s-polarized wave's original energy (E_s) gets reflected (R_s), see Equation 2.2a. Using Snell's law, we can simplify the equation to Equation 2.2b, which now only relies on the angles present and not the materials themselves [Gol16].

A similar approach can be taken to calculate the amount of the wave that is transmitted within the material (T_s), see Equation 2.3a. We can use Snell's law here as well, resulting in Equation 2.3b [Gol16].

$$R_s = \frac{n_1 cos\theta_i - n_2 cos\theta_r}{n_1 cos\theta_i + n_2 cos\theta_r} E_s \tag{2.2a}$$

$$R_s = -\frac{sin(\theta_i - \theta_r)}{sin(\theta_i + \theta_r)} E_s \tag{2.2b}$$

$$T_s = \frac{2n_1 cos\theta_i}{n_1 cos\theta_i + n_2 cos\theta_r} E_s \tag{2.3a}$$

$$T_s = \frac{2sin\theta_r cos\theta_i}{sin(\theta_i + \theta_r)} E_s \tag{2.3b}$$

The energy of the incoming ray has to be equal to the sum of reflected, transmitted and absorbed component, see Equation 2.4. For mirror-like surfaces, such as water, the absorbed component is negligible.

$$E = R + T + A \tag{2.4}$$

For **p-polarized** light, the electric field vector is parallel to the plane of incidence. Again, using the Fresnel equations and Snell's law, we can calculate the reflection and transmission amplitudes.

With the values for θ_i and θ_r, as well as the energy of wave E_p, we can calculate the reflection with and without the refractive indices, see Equation 2.5a and Equation 2.5b, respectively. The same goes for the transmission, see Equation 2.6a and Equation 2.6b [Gol16].

$$R_p = \frac{n_2 cos\theta_i - n_1 cos\theta_r}{n_2 cos\theta_i + n_1 cos\theta_r} E_p \tag{2.5a}$$

$$R_p = \frac{tan(\theta_i - \theta_r)}{tan(\theta_i + \theta_r)} E_p \tag{2.5b}$$

$$T_p = \frac{2n_1 cos\theta_i}{n_1 cos\theta_i + n_2 cos\theta_r} E_p \tag{2.6a}$$

$$T_p = \frac{2sin\theta_r cos\theta_i}{sin(\theta_i + \theta_r)cos(\theta_i - \theta_r)} E_p \tag{2.6b}$$

Equation 2.4 holds here as well.

It has to be mentioned that the Fresnel equations used here are simplified, since we assume that both materials are non-magnetic [BW13]. This is generally the case for the mediums that we are interested in, water and air. While the equations only work for s- and p-polarization, there are more cases; waves can have elliptical polarization or are oriented linearly at an angle in between s and p. This is not a problem however, since we can decompose the polarization mathematically into the respective amounts of s and p.

One special case which can be derived from the previously mentioned equations is **Brewster's angle** θ_B. In this case, the transmission of p-polarized light and the reflection of s-polarized light are maximized. This means that the reflected waves are completely polarized, parallel to the surface. Brewsters angle is defined as shown in Equation 2.7a. This is due to the fact that this effect occurs when the sum of θ_i and θ_r is 90°, see Equation 2.7b [San65].

$$\theta_B = arctan\left(\frac{n_2}{n_1}\right) \tag{2.7a}$$

$$90° = \theta_i + \theta_r \tag{2.7b}$$

In the case of Equation 2.5b, we can substitute Equation 2.7b and get Equation 2.8.

$$R_p = \frac{tan(\theta_i - \theta_r)}{tan(90°)} E_p \tag{2.8}$$

Since $tan(90°)$ is undefined, we get no value for the reflection of p-polarized light. Using Equation 2.4, we can state that all of the p-polarized light gets transmitted rather than reflected. Therefore, all the remaining reflected light can only be s-polarized and is consequently linearly polarized [Sai+99].

Knowing how much s- and p-polarized light is reflected enables establishing the metric Degree of Polarization (DOP), as defined in Equation 2.9 [Zho+17].

$$\mathrm{DOP}_r = \frac{r_s^2 - r_p^2}{r_s^2 + r_p^2} \tag{2.9}$$

In the case of Brewster's angle, we therefore get a DOP_r value of 1, see Equation 2.10.

$$\mathrm{DOP}_{rB} = \frac{r_s^2 - r_p^2}{r_s^2 + r_p^2} = \frac{r_s^2 - 0^2}{r_s^2 + 0^2} = \frac{r_s^2}{r_s^2} = 1 \tag{2.10}$$

The relation of the DOP_r to the angle of incidence can be seen in Figure 2.7, for the specific case of a water-air interface. One can see that the highest amount of DOP_r is reached at Brewster's angle, which is at 53.1°, while there is no polarization beyond 90° [She+17].
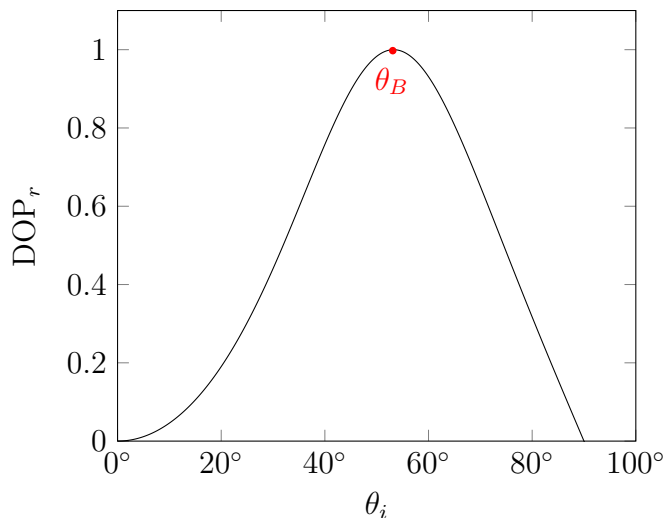
Figure 2.7: Degree of Polarization for the reflection at a water-air interface, depending on the angle of incidence θ_i, assuming initially unpolarized light.

2.1.3 Stokes Parameters

One way to express polarization mathematically is to use the Stokes Parameters. With four different values s_0, s_1, s_2 and s_3 one can completely describe polarization. The first parameter, s_0, describes the general intensity of the wave. s_1 determines the difference between the vertical and horizontal components, s_2 for the diagonal ones. Circular polarization is expressed in s_3 [Li+14].

2.1.4 Atmospheric Polarization

Figure 2.7 assumes unpolarized light, meaning that E_p is equal to E_s. While this is generally a good assumption for natural light, most light in nature is normally partially polarized.

This seems contradictory to a previous statement, saying that light emitted by natural sources is generally unpolarized. However, light is scattered in the upper atmosphere due to molecules and aerosols which introduces a certain degree of polarization [Zho+17]. This effect is called **Rayleigh scattering**.

In general it states that when a light wave interacts with a molecule, it will re-radiate the energy in such a way that the light that reaches the observer is (partially) polarized.

In order to calculate the specific orientation, four values are needed: The *zenith* and *azimuth* of the sun and the observed point. Note that the following description of Rayleigh scattering assumes clear sky, since clouds change this behaviour [Gol16].

The azimuth ψ, as shown in Figure 2.8, states how far a point is away from the reference point, generally true north. This means, for example, that south would be at 180° and east at 90° if one were to choose north as the reference point. The zenith is reached when the object is directly above the observer, meaning 90° above the horizon. The zenith angle θ is therefore how far the object is away from the zenith. Any value larger than 90° means that the object would be below the horizon.
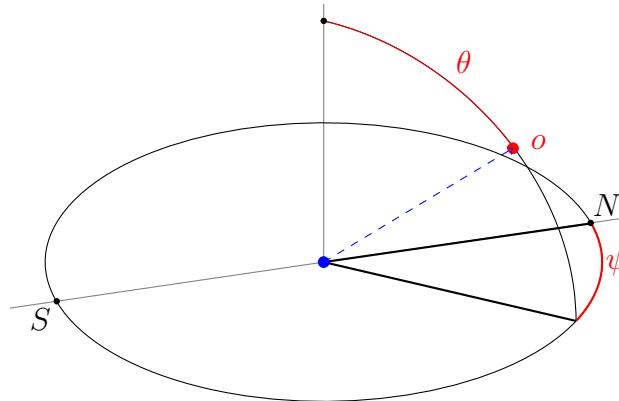
Figure 2.8: Azimuth ψ and zenith angle θ, from an observer to an observed point o.

Using the azimuth for the sun ψ_s and the observed point ψ_o as well as the zenith angle θ_s for the sun and θ_o for the observed point, one can calculate the scattering angle γ, using Equation 2.11 [Zho+17].

$$\cos\gamma = \sin\theta_s \sin\theta_o \cos(\psi_o - \psi_s) + \cos\theta_s \cos\theta_o \tag{2.11}$$

The scattering angle is the angular difference between the position of the sun and the position of the observed object.

Using the value for γ, we can calculate the DOP, see Equation 2.12. Theoretically, this value can reach 100%. However, a real world setting introduces additional

atmospheric conditions that limit the DOP to around 77%, represented by the value DOP_{max}.

$$DOP = DOP_{max} \frac{\sin^2 \gamma}{1 + \cos^2 \gamma} \tag{2.12}$$

The equation shows that the highest DOP can be reached for a scattering angle of 90°, while the lowest value is reached at 0° and 180°.

With Equations 2.11 and 2.12 we can now calculate how high the degree of polarization should be at a given position in the sky. Here, the relative azimuth angle ψ_r is the shortest angular distance between ψ_o and ψ_s This is not the same as the scattering angle. Figure 2.9 shows the theoretical DOP pattern in the sky. Note that the max DOP here is 1.

Figure 2.9: The DOP in the sky, for a given ψ_s of 0° and a fixed θ_o of 90° in relation to a changing observer azimuth and solar zenith.

Additionally, we can also use the values for ψ and θ to calculate the AOP at that particular position, see Equation 2.13 [Wan+14]. Here, the numerator represents the p-polarized portion and the denominator the s-polarized part.

$$\tan(AOP) = \frac{\cos \theta_s \sin \theta_o - \sin \theta_s \cos \theta_o \cos(\psi_o - \psi_s)}{-\sin(\psi_o - \psi_s) \sin \theta_s} \tag{2.13}$$

The theoretical sky polarization pattern can be seen in Figure 2.10.

We can see that the AOP changes sign as we pass the solar meridian. Note that while the contrast at ±180° seems very high, 90° and −90° are basically interchangeable, since we can only ever have angles in the range of $[0, 180]$.
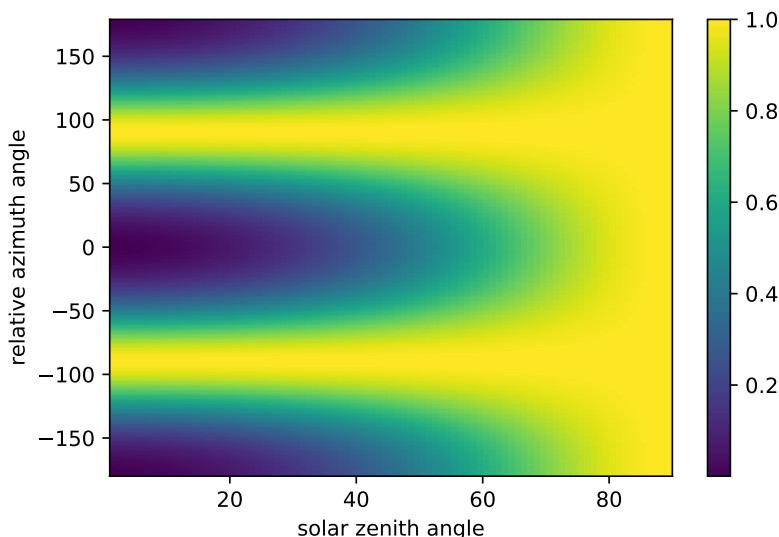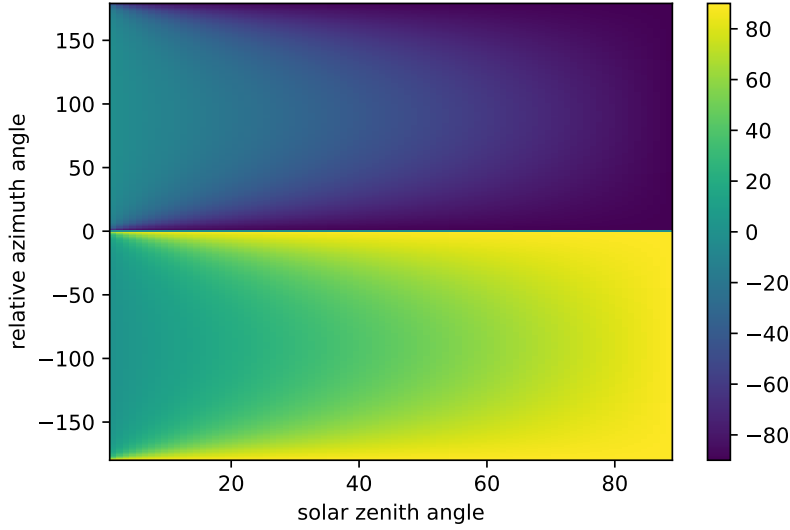
Figure 2.10: The AOP in the sky, for a given ψ_s of 0° and θ_o of 90° in relation to a changing observer azimuth and solar zenith.

2.1.5 Reflecting Polarized Sky Light

Knowing how water reflects polarized light as well as being able to calculate the polarization of light at a specific point in the sky enables the calculation of the DOP on a water surface.

Since one will generally face downwards towards a reflective surface, the zenith of the observed point in the sky can be established by subtracting the angle of incidence from 90°. By using the angle of incidence with the Fresnel equations, we can calculate how much of the incident s- and p-polarized waves get reflected, see Equations 2.1, 2.2b and 2.5b. However, we need to establish E_p and E_s as well, since the sky light is not unpolarized.

The proportions of the incoming s- and p-waves E_s^S and E_p^S are a combination of actually polarized light waves and unpolarized light waves.

We can calculate the actually polarized components by decomposing the AOP into the respective amounts of s- and p-polarized waves E_s^{pol} and E_p^{pol}, see Equations 2.13 and 2.14.

$$
\begin{aligned}
E_s^{pol} &= -\sin(\psi_o - \psi_s)\sin\theta_s \\
E_p^{pol} &= \cos\theta_s\sin\theta_o - \sin\theta_s\cos\theta_o\cos(\psi_o - \psi_s)
\end{aligned}
\tag{2.14}
$$

The two values are then normalized, see Equation 2.15.

$$
\begin{aligned}
E_s^{pol} &= \frac{E_s^{pol}}{E_s^{pol} + E_p^{pol}} \\
E_p^{pol} &= \frac{E_p^{pol}}{E_s^{pol} + E_p^{pol}}
\end{aligned}
\tag{2.15}
$$

The proportion of s- and p-polarized waves in unpolarized light is 50:50 due to the random orientation of the waves. By calculating the DOP at the observed point, we

know how much unpolarized light there is and set that into relation to the already calculated linearly polarized light, see Equation 2.16.

$$E_s = \text{DOP} * E_s^{pol} + \frac{1 - \text{DOP}}{2}$$
$$E_p = \text{DOP} * E_p^{pol} + \frac{1 - \text{DOP}}{2}$$

(2.16)

By then calculating the DOP as a fraction of s- and p-polarized light, the theoretical value at the water surface is known, see Equation 2.9.

2.1.6 Polarizing Filters

In order to detect what kind of polarized light is occurring, one can deploy polarization filters, also known as polarizers. The term polarizer is in so far fitting, as that it converts unpolarized light into one particular orientation. While there are different types of filters, we will only discuss wire-grid polarizers, since they are used in the IMX250MZR.

Wire-grid polarizers are a form of polarizing filter that deploy nano-sized metal wires. The wires are parallel to each other and conduct electricity [Hec13]. Broadly speaking, the filter works by only allowing light in a particular orientation to pass. Going back to s- and p-polarized components, we can refer to original wave as two waves - one that moves perpendicular to the wires and the other one parallel.

P-polarized waves move along the wires, transferring their energy to the atoms in the wire. Since they are parallel, there is enough time and distance for the intersecting wave to actually transfer most of its energy. The wave then gets re-radiated by the wire and interferes with the part of the original wave that passed through the wires, thus removing most of the p-polarized wave [Hec13].

On the other hand, s-polarized waves have less impact with the grid, since their direction is perpendicular to the wires. Less energy gets transferred and the wave can propagate more or less unaltered through the grid. [Hec13].

This means that a wire-grid will only transmit radiation that is perpendicular to its own orientation, as can be seen in Figure 2.11. There are other factors that influence how much of the wave is getting transmitted, such as the incidence angle and how much of the energy is transformed into heat in the wires of the grid itself [YK03].
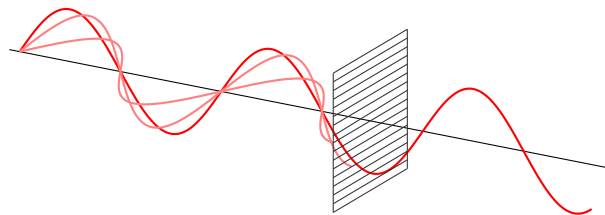
Figure 2.11: Differently polarized waves arrive at a wire-gird polarizer. Only the wave with orientation perpendicular to the grid is transmitted.

2.2 Stereo Vision

In Stereo Vision, one can construct a three dimensional description of a scene by observing said scene from different perspectives [MMK13]. Generally speaking, the scene will be observed by two cameras, placed at slightly different positions [MV08].

2.2.1 Stereo Distance Measurement

In order to enable further processing, one needs to adhere to two particular restrictions [MV08]: The images need to be horizontally aligned and be taken at the same instant.

We can refer to the pictures as **Stereoscopic pictures**. It is important that the cameras share the same features, such a focal length f and view angle φ_0 [MMK13]. In order to calculate the distance between the cameras and an object, additional metrics are necessary.

First, the location of the object O in each image has to be established. For that, the distance from the middle of the picture can be used, x_l and x_r respectively, see Figure 2.12. The x values are given in pixels, x_0 being the width of the image itself.
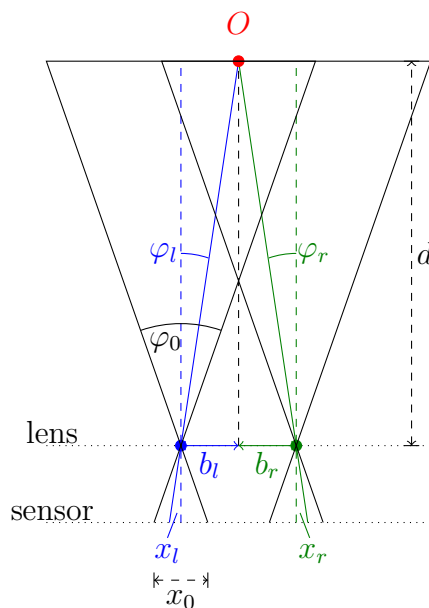
Figure 2.12: Parameters for estimating the distance to an object 0, as seen by two cameras simultaneously.

The value b_0 refers to the distance between the cameras. This value is generally constant, since the cameras should not moved during use within the setup. Additionally, we refer to the distance between each cameras center view point and the object itself as b_l and b_r. We can use those values for basic triangulation in order to

calculate the distance d, see Equation 2.17 [MMK13].

$$b_0 = b_r + b_l = d \tan \varphi_l + d \tan \varphi_r$$
$$d = \frac{b_0}{\tan \varphi_l + \tan \varphi_r} \tag{2.17}$$

The viewing angle φ can be established using x, see Equation 2.18.

$$\frac{x_l}{\frac{x_0}{2}} = \frac{\tan \varphi_l}{\tan \frac{\varphi_0}{2}}$$
$$\frac{-x_r}{\frac{x_0}{2}} = \frac{\tan \varphi_r}{\tan \frac{\varphi_0}{2}} \tag{2.18}$$

Using Equations 2.17 and 2.18 we can calculate the distance d. In order to compensate for alignments errors, we also introduce the alignment compensation term ϕ, which adjusts the viewing angle, see Equation 2.19. This is necessary, since the cameras will most likely not be aligned perfectly inhowever a real world setting.

$$d = \frac{b_0 x_0}{2 \tan \left(\frac{\varphi_0}{2} + \phi \right) (x_r - x_l)} \tag{2.19}$$

With the camera's focal length f, we can express the distance equation in a simpler way, see Equation 2.20.

$$d = \frac{f b_0}{(x_r - x_l)} \tag{2.20}$$

By incrementing the distance b between the cameras, the long-range accuracy increases [MV08]. In general, the accuracy of the distance measurement is higher when the particular object is closer. This is due to the inverse relationship between the pixel disparity and the distance of the object [Bag09].

2.2.2 General Disparity Estimation

This methods works well for a single target which has been annotated in both the left and the right picture. The general problem is a more complex one: For any point in the one image, the corresponding point in the other image has to be identified or *matched* [HI16]. This is particularly hard since not all points may have a visible counterpart in the other image, due to occlusion.

In order to discuss matching algorithms, it is necessary to establish certain terms. We use two images I_l and I_r. For any point P, p_l and p_r represent matching brightness values or intensities in the respective image. In real world geometry, those values lie on the same horizontal line e. Working under this assumption reduces computational load, since the matching algorithm does not have to search the whole image for similar values [HI16].

Generally speaking, this is not possible with regular images. The camera's lens introduces a certain amount of distortion, the two cameras might also not be aligned perfectly. The process of reverting the distortion and a the alignment errors is called **rectification** [Sze10].

Rectification works by rotating, distorting and translating the image based on a

fixed ground truth object, such as a chessboard. By knowing the exact dimensions and the fact that the lines between the corners on the board are straight in the real world, a set of parameters intrinsic to the camera can be established. This set of parameters is referred to as the Q-Matrix. This matrix contains the estimated distance between the two camera center points, as well as the supposed focal length. The quality of the calibration process is measured in as the pixel reprojection error. It is calculated by reprojecting a point in the image by using the previously established parameters. Knowing where that value is in 3D space through the chessboard results in an error value. The lower the value, the better the rectification parameters [HZ03].

We will assume rectified images from now on, in order to simplify the process of stereo matching.
After having set up the images, the disparity can be calculated. One way to do so is by using a cost model. The cost measures how much a pixel in the original image would have to be moved in order to find it in the target image, at a position of similar intensity. This calculation will then be executed for each pixel in question. [HI16].
One frequently used algorithm is the Sum of Absolute Differences (SAD). Rather than looking at each individual pixel, it calculates the cost within blocks. This enables a more robust calculation, since outliers within a block are accommodated for. The algorithm will calculate the absolute intensity difference between the block in the left image w and the block in the right image. Equation 2.21 shows the cost calculation for two particular blocks. The block in the left image is translated by d, being the disparity. We only need to translate the blocks in the direction of x, due to the fact that both blocks should lie on e.
The step from SAD to actual matching is an optimization problem. We try to minimize the SAD value when matching p_l on p_r. The lowest SAD value then gives us the disparity value for that particular block.

$$\text{SAD}(x, y, d) = \sum_{(x,y)\in w} |I_l(x, y) - I_r(x - d, y)| \tag{2.21}$$

This approach assumes that all the pixels in the window have the same disparity values. Depending on the window size, this can lead to fast, but fuzzy measurements [LS11]. Having calculated the disparity map, we can calculate the real world distances now with Equation 2.20. This is possible since we also know the focal length of the camera as well as the distance between the two cameras due to the previously established Q-matrix.

3
Methods

This chapter contains the explanation of various elements needed for water detection. It also touches on different experiments which were conducted in order to gather information on how the polarization behaves in relation to the position of the sun and the surrounding area. Finally, an algorithm for water detection is proposed.

3.1 Setup

The IMX250MZR is a polarization image sensor. Rather than having a polarizing filter in front of the lens, as an accessory, this sensor features differently aligned wire-grids on a per pixel basis [Son18]. This type of filtering is called filter on chip (FOC) [RRN19].

The filters are aligned in four different orientations: 0, 45, 90 and 135°. We will refer to specific alignments as I_n with $n \in \{0, 45, 90, 135\}$ respectively. They are combined in a 2x2 matrix, see Figure 3.1. The data is recorded in grayscale.
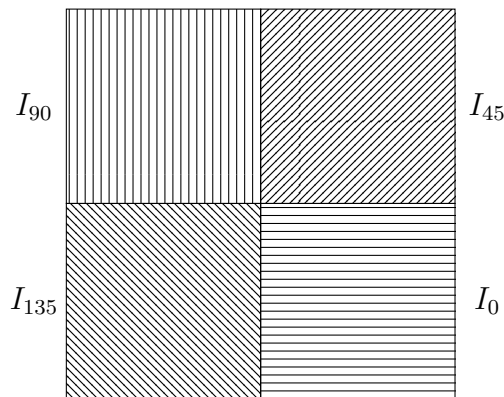
Figure 3.1: 2x2 pixel grid with differently aligned grids as used on the IMX250MZR.

If 0° linearly polarized light were to arrive at the pixel grid, each pixel in the grid would register a different value, as can be seen in Table 3.1. Notice how I_0 registers no intensity, since the wire grid polarizers only transmit light that is polarized perpendicular to the wires. The diagonal polarizers register only half of the original intensity, since the wave can be broken down into 50 % s- and 50 % p-polarized light.

Table 3.1: Theoretical intensities for four differently aligned polarizers for 0° linearly polarized light.

Polarizer	Intensity (%)
I_0	0 %
I_{45}	50 %
I_{90}	100 %
I_{135}	50 %

In real life, additional constraints on the sensor inhibit this behavior, such as issues in manufacturing.

For the purpose of this thesis, IMX250MZR has been fitted with a lens with a focal length of 35mm. A higher focal length generally means that the camera has a smaller field of view and a higher magnification, and vice versa.This specific focal length provides a compromise between having a high enough resolution at a distance, while also having information about closer objects.

This compromise has also been struck when it comes to the placement of the cameras in a stereo setup. They have been mounted on a rod, about 51cm apart. This provides reasonable disparity resolution at a distance, while still allowing for stereo matching on closer distances.

3.2 Basic Components

While the IMX250MZR does provide 12 bit depth for the recorded images, some image processing functions, as provided by OpenCV [Bra00], require the source image to have a depth of 8 bit. Since the 12 bit depth image provides more information, it will be used where possible. Otherwise, the image will be converted accordingly.

3.2.1 Preprocessing

As previously mentioned, the sensor does provide the four polarization directions on a per-grid basis. However, it is more convenient and intuitive to work with a different setup: Having the phases as a channel on a per-pixel basis. So rather than having one grayscale value per pixel, we want to work with four different values per pixel, each relating to a single polarizer. The sensor does not provide the data in that way, so it is necessary to process it. In order to extract the different phases, two approaches can taken.

First, one could handle the 2x2 grid as a single computational unit and simply use each (sub-)pixel as input for the particular channel. This approach is easy to implement and produces only a relatively small computational load. This also reduces the resolution of the image by a factor of four, since we combine four pixels into one. The reduced resolution of course also reduces the computational load for further processing, since less pixels have to be handled. However, a high resolution is beneficial for a more accurate distance measurement at a longer distance.

Therefore, it is necessary to enhance the image in such a way that we can keep

the high resolution, but also provide the four channels. This can be achieved using custom interpolation, as the second option.

For each pixel, we need to calculate the four phases using the surrounding pixels. Due to the nature of the grid, we only need to look in a 3x3 grid around the pixel we are currently handling. There, depending on the original orientation of the current pixel, we can calculate the values for the other phases as well, see Figure 3.2.
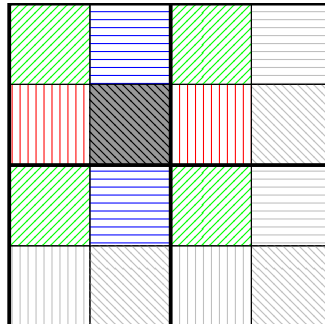

Figure 3.2: Source pixels for interpolation per phase on the pixel marked in gray. The light gray pixels on the side are part of the specific 2x2 grid, but not used for the interpolation of the given pixel.

In order to interpolate the entire image, this interpolation grid will simply be applied to all the pixels in the image. Afterwards, each pixel holds the interpolated polarization intensities in four distinct channels.

3.2.2 Distance Measurements

In order to provide a accurate distance measurements it is necessary to apply the tools and algorithms mentioned previously in Section 2.2.

Due to the sensor's pixel layout, neighboring pixel values do not represent the real world brightness of that particular point. This quick change in value could be detrimental to stereo matching algorithms, which rely on similar intensity levels in order to match the pixels in the left image to the ones on the right.

It is therefore beneficial to use the previously mentioned interpolated image. For ease of calculation, one can combine the four channels in to a single one in order to provide a conventional gray scale image, see Figure 3.3.

In that figure, the images have been deliberately offset vertically by mounting the cameras at a slight different angle, in order to demonstrate the effects of stereo rectification.

Having processed the images, we now apply stereo calibration and rectification algorithms in order to prepare the images for the matching step. An example of rectified images can be seen in Figure 3.4. Notice how the translation and rotation of the images created black margins and how the images are now aligned vertically.

With the images rectified, we can now apply Stereo matching. The matching step only produces a sparse disparity map, since not all points in the image could be matched. This causes artifacts, as can be seen in Figure 3.5. The gaps can be filled by using a disparity filter, which applies the weighted least squares algorithm.

Figure 3.3: Example images for the stereo calibration, with the chessboard present.

Figure 3.4: The images from Figure 3.3 after applying the rectification.

After applying said filter, the disparity map is now dense and can be used for further distance calculation, see Figure 3.6. Notice how the filtered map is less fractured and more even. It also deals better with occlusion, mostly noticeable when comparing the values left of the person holding the chessboard.

The matching works reasonably well with the images shown: They are high in texture, which means that the matcher has enough features to match one point to another. This can be seen in the clear edges in the disparity map in Figure 3.6.
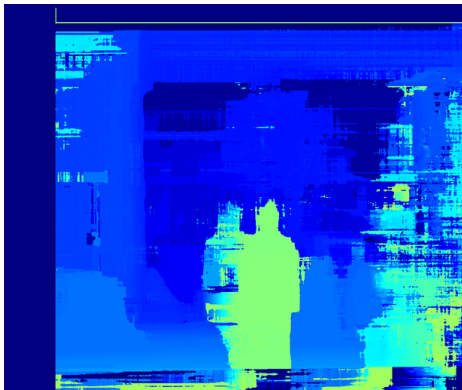
Figure 3.5: The unfiltered disparity map for Figure 3.3
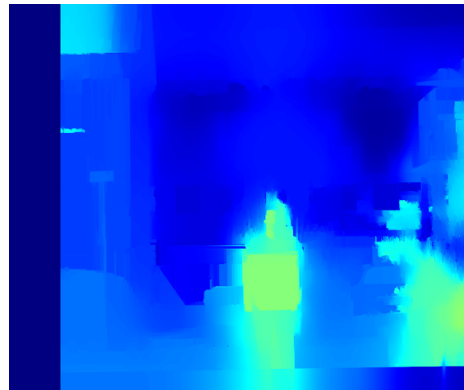
Figure 3.6: The filtered disparity map for Figure 3.3

3.2.3 Calculating the Stokes Parameters

In order to calculate the AOP and DOP later, we need to establish the Stokes parameters based on the intensity values from the different polarizers first. Since it is only possible to detect partial linear polarization with the IMX250MZR due the nature of the wire grid, we can not calculate s_3. The other parameters can be established as can be seen in Equation 3.1 [She+17]. The initial phase intensities need to be normalized to the interval $[0, 1]$ beforehand.

$$
\begin{aligned}
i_0, i_{45}, i_{90}, i_{135} &\in [0, \dots, 1] \\
s_0 &= \frac{i_0 + i_{45} + i_{90} + i_{135}}{2} \\
s_1 &= i_0 - i_{90} \\
s_2 &= i_{45} - i_{135}
\end{aligned}
\tag{3.1}
$$

3.2.4 Calculating the Angle of Polarization

The angle of polarization is, as mentioned in Subsection 2.1.1, the angle between the linearly polarized light wave and a reference plane. The reference plane in our case is the horizontal plane through the two cameras.

We can use the Stokes parameters to calculate the AOP, see Equation 3.2 [HMD14]. The sgn function extracts the sign of the given number, either positive or negative.

$$
\begin{aligned}
s_1 = 0 \quad &\begin{cases} s_2 > 0 : & \pi/4 \\ s_2 = 0 : & \textit{only relevant for circular polarization} \\ s_2 < 0 : & 3\pi/4 \end{cases} \\
\chi &= \arctan \frac{s_2}{s_1} \\
s_1 \neq 0 \quad &\begin{cases} \operatorname{sgn}(\chi) = \operatorname{sgn}(s_1) : & \chi \\ \operatorname{sgn}(\chi) = - \wedge \operatorname{sgn}(s_1) = + : & \chi - \pi/2 \\ \operatorname{sgn}(\chi) = + \wedge \operatorname{sgn}(s_1) = - : & \chi + \pi/2 \end{cases}
\end{aligned}
\tag{3.2}
$$

Equation 3.2 does produce values in the interval $[-45°, 135°]$. In order to reach the more intuitive interval of $[0, 180]$, 180 is added to any negative angle.

3.2.5 Calculating the Degree of Polarization

Similar to the AOP, we can calculate the DOP by using the Stokes parameters, see Equation 3.3 [She+17].

$$\text{DOP} = \frac{\sqrt{s_1{}^2 + s_2{}^2 + s_3{}^2}}{s_0} \tag{3.3}$$

Since s_3 is not defined in our case due to the wire grid polarizers on the IMX250MZR, we can omit it. The result is the fraction of polarized light in relation to the total intensity.

3.2.6 Solar Position Estimation

The position of the sun differs depending on the time of day, as well as the specific day of the year. In order to use it as a cue for segmentation, the position needs to be calculated depending on the location of the observer as well as the current time. By using the position of the observer, given in latitude and longitude, as well as the Coordinated Universal Time (UTC) at the desired point in time, one can calculate the ψ_s and θ_s for the given parameters [Mee91].

3.2.7 Segmentation

The goal of segmentation is to identify regions with different features in an image. Normally, the image will be pre-processed to enhance the image in such a way that the requested features are more easily detectable. One of the most common way to do so, is to apply a threshold to an image. Any pixel value that is below the threshold will receive the value 0, the rest 1. That transforms the image into a binary image.

Depending on the feature one wants to extract, this process needs to be repeated multiple times with differently prepared images, adding or subtracting the resulting images.

The underlying assumption for using segmentation in this thesis is that water is differently polarized than the rest of the scene.

3.3 Experiments

With the basic tools for detecting polarized light in place, it is necessary to see how they can be used in the real world in order to detect water hazards. For this, a couple of experiments were conducted.

With the results from the experiments, we can compare the measured values with the theoretical values, according to the Rayleigh sky polarization model. This also gives a first insight into the influence of the sun on the polarization on the ground.

Similar experiments have been conducted previously, for example [She+17]. They used an inverted setup, meaning that they placed a non-reflective surface on water. Additionally, they did not measure polarization by itself but the contrast between said object and the water, depending on the position of the camera and the sun. Subsection 3.3.3 differs in that regard since it aims at replicating previous results and evaluating the feasibility of applying the given algorithm to an urban environment.

3.3.1 Influence of the Sun on the Degree of Polarization

As already mentioned in Subsection 2.1.4, the position of the sun influences the polarization of the light for a particular observer, especially when looking at the sky. In order to test how this phenomenon affects polarization on the ground, the following experiment was conducted.

A bowl, filled with a dark liquid, in this case coffee, was placed on the ground, in this case asphalt, in order to emulate a fixed water surface on the street. The dark liquid was used in order to reduce the amount of internal reflection, more on this later. The cameras were then focused on the liquid and used to take pictures of the bowl from different angles, see Figure 3.7. The assumption is that the liquid will reflect the sky at a certain position, which will influence the polarization. In the test setup, ψ_s was around $220°$ and θ_s at $45°$. ψ_o will change from image to image, whereas θ_o was kept at around $45°$. Note that all of the images were taken during clear sky, in order to rely on the Rayleigh sky polarization model.
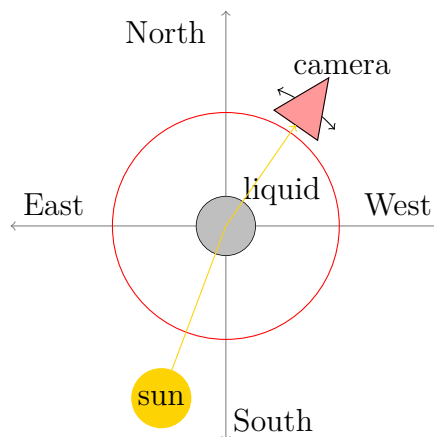
Figure 3.7: Test setup for measuring the DOP in relation ψ_r.

First, the composition of the theoretical DOP at the surface of the liquid, DOP_L^t will be investigated. We can calculate the value by knowing the angle of incidence as well as the polarization in the sky at the reflected point. The angle of incidence θ_i here is the same as θ_o, due to the reflection. We also need to consider AOP_{sky}, the value of the AOP at the given point in the sky, as well as DOP_{sky}.

The results can be seen in Table 3.2. One can see that DOP_L^t increases with a decrease in DOP_{sky}. Additionally, AOP_{sky} is generally closer to $90°$ along the solar meridian than it is to the diagonals at $45°$ and $135°$. This means that proportion of

s-polarized waves is higher in the unpolarized component rather than in the linearly polarized one.

The behaviour of DOP_L^t can be explained by comparing three cases, a relative angle of 175°, 130° and −5°.

In the first case, the AOP_{sky} of 86.47° consists of a large amount of p-polarized light. This means that most of s-polarized component, which is the one that will be reflected, is contributed by the unpolarized light. Since that value is relatively low due to the high DOP_{sky}, DOP_L^t is low.

In the case of 130°, we do have a similar DOP_{sky} value. Yet here, the AOP is further away from 90°, which increases the proportion of the s-polarized wave significantly. Combining that with a marginally lower DOP_{sky} results in the large difference in DOP_L^t. Comparing the relative angles of −5° and 175°, the AOP_{sky} is basically the same amount off 90°, which makes the proportions of s- and p-polarized waves very similar. Yet here, the DOP_{sky} is extremely low, which means that the largest contributor to the s-polarized portion is the unpolarized component, which has a higher fraction of the s-polarized wave to begin with.

Table 3.2: Comparison between DOP_{sky}, AOP_{sky} and DOP_L^t at a air-water interface with θ_s and θ_o of 45°. The relative azimuth angle ψ_r is the angle between ψ_s at 220° and ψ_o.

ψ_r (°)	DOP_{sky} (%)	AOP_{sky} (°)	DOP_L^t (%)
175	66.50	86.47	28.5
130	62.39	61.51	76.8
85	36.16	54.79	86.6
40	8.23	65.52	88.4
-5	0.13	93.53	89.9
-50	12.92	118.49	88.0
-95	43.57	125.21	85.8
-140	64.70	114.48	70.1

Knowing the theoretical value, we can compare it to the value that the camera actually registered. We also introduce DOP_L^r, the actual value of the DOP at the surface of the liquid, as well as DOP_S, the DOP value of the surrounding surface, in this case asphalt. The results can be seen in Table 3.3.

In accordance with the theory, DOP_L^r is generally higher when the observer is facing the sun. This is also the case for DOP_S, even though the values are significantly lower.

However, DOP_L^r is generally lower than DOP_L^t. This might be caused by additional atmospheric conditions or that the liquid was not perfectly flat due to wind. Also, DOP_L^r is higher than expected when facing away from the sun. This might also be caused by the previously mentioned issues.

Remarks The experiment was first conducted with clear water in a white ceramic bowl. In that particular case, the results showed the DOP of the bowl was lower

Table 3.3: Comparison of the DOP in relation to ψ_r. ψ_s was 220° at the time of measurement, θ_s and θ_o at 45°

ψ_r (°)	DOP_L^r (%)	DOP_S (%)	DOP_L^t (%)
175	33.1	3.6	28.5
130	24.2	4.0	76.8
85	29.9	10.0	86.6
40	54.9	19.4	88.4
-5	65.6	23.4	89.9
-50	41.9	16.3	88.0
-95	27.2	5.8	85.8
-140	27	4.4	70.1

than the one of the surrounding area. In theory, it should be higher due to the fact that a larger fraction of s-polarized light is reflected than the fraction of p-polarized light.

The lower DOP therefore means that more p-polarized light was registered on the surface than expected. We assume that this is the case due to reflections within the liquid itself.

Normally, water on the street is not as clear as water from the tap. The asphalt on the street is also not as smooth or reflective as a white ceramic bowl. Therefore, a darker liquid within a darker bowl was chosen in order to emulate a street in an controlled environment.

Also, the incidence angle of 45° is higher than the angle if looking at a distance. However, the change in value is not that important, since the experiments are focused on the trends rather than actual values.

3.3.2 Influence of the Sun on the Angle of Polarization

The experiment from Subsection 3.3.1 was repeated, this time with a focus on the AOP. For a more intuitive comparison of the AOP, the interval $[0, 180]$ has been transformed to the interval $[-90, 90]$, meaning that an angle of 170° is now expressed as $-10°$. The results can be seen in Table 3.4.

One can see that AOP_L is relatively close to 0, as was to be expected. The difference between AOP_L and AOP_S appears to be largest when facing 90° away from the sun. Along the solar meridian, the two values are quite close to each other and are likely not usable for segmentation.

3.3.3 Similarity Degree

Bin Xie et al. deploy a so-called similarity degree S in order to detect water hazards. It expresses how similar the angles in a particular window are compared to the center pixel of the window. This works under the assumption that the light on water surface is more similarly polarized compared to the rest of the scene.

For a particular pixel in the image at position (x, y), S is defined as in Equa-

Table 3.4: Comparison of the AOP in relation to the solar azimuth and the observer azimuth. The solar azimuth was 220° at the time of measurement, the zenith 45°, with a fixed observer zenith of 45°.

ψ_r (°)	AOP_L (°)	AOP_S (°)
175	-0.76	-2.87
130	1.56	-40.78
85	-2.43	-41.24
40	-5.26	-23.19
-5	-3.87	3.55
-50	17.47	22.16
-95	-6.95	37.03
-140	-3.85	-0.51

tion 3.4, with $\mathrm{AOP}(x, y)$ being the angle of polarization at the particular position and $\overline{\mathrm{AOP}(x, y, w)}$ being the average of the angle of polarization in a window of size w with center point (x, y) [Bin+07].

$$S(x, y, w) = |\, \mathrm{AOP}(x, y) - \overline{\mathrm{AOP}(x, y, w)}| \tag{3.4}$$

A lower value denotes a more similar window. After establishing S for the entire image, an adaptive threshold based on the min and max values of S is applied. Applying this algorithm to test images taken in an urban environment resulted in poor results. The similarity of the surrounding area was not low enough for it to not be considered water in comparison with the actual water surface. It was possible to identify vegetation on the side of the road however.

This means that the similarity degree, as implemented here, does not provide the necessary insight into the difference between water and asphalt to be useful for water detection in an urban environment.

3.4 Water Detection

With the different components in place, a combination of them is needed in order to reliably recognize water surfaces. This section will show how the components can be used in order to detect water hazards. Two example images will be used in order to show the effect of the individual steps. They can be seen in Figure 3.8, with the water hazard ground truth marked in red. We will be referring to the left image as `image_1` and the right one as `image_2`. `image_1` was taken with $\psi_r = -152°$ and $\theta_s = 25°$, `image_2` with $\psi_r = 27°$ and $\theta_s = 25°$ as well. Just like all images, both were taken during clear skies.

By choosing those particular angles, the camera is either facing towards or away from the sun. The large difference in polarization is visible in the two images, which is why they have been selected for this visualization. Note that an in-depth analysis with images from additional angles will be given in Chapter 5.

Figure 3.8: Original input images for the water detection algorithm. Water hazards are marked in red.

3.4.1 Segmentation Based on the Degree of Polarization

As the experiments showed, the DOP can be used to segment water surfaces from the rest of the scene. However, the experiments also showed that a single, general purpose threshold would not work, since the values change depending on the relative angle of the observer and the sun. The DOP seemed to depend on ψ_r, which will therefore be used an indication for the threshold.

In order to establish the current relative angle between the camera and the sun, three parameters are needed: First, the current location of the observer, the observer azimuth of the camera as well as the current time of day. All of these can be established by using a global navigation satellite system (GNSS), such as GPS.

Using the ψ_r, a threshold for the DOP can be chosen based on previous, empiric results.

In Figure 3.9 one can see the DOP false-colour image of the original images.
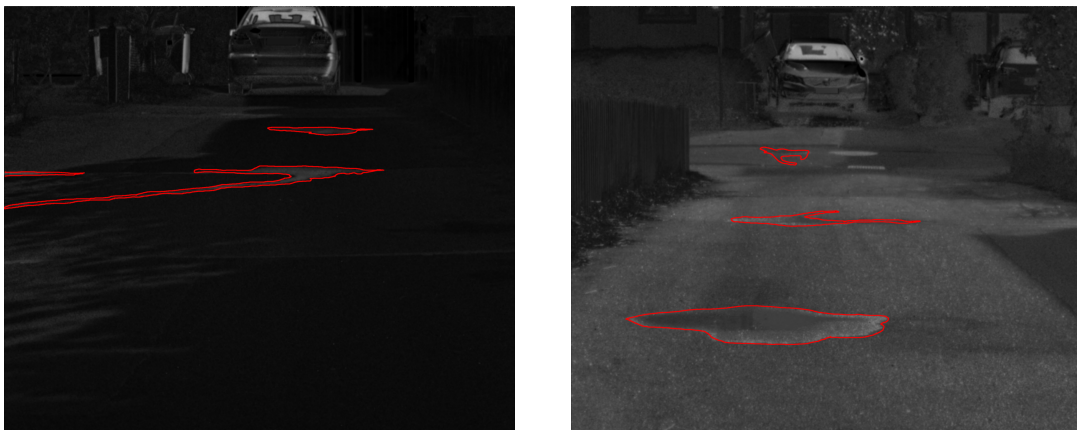

Figure 3.9: DOP false colour images for the water detection algorithm. Water hazards are marked in red. A higher pixel value corresponds to a higher DOP

Before the empirically determined threshold is applied, the image is blurred. This decreases noise and results in a more coherent image after applying the threshold. The resulting binary image can be seen in Figure 3.10.
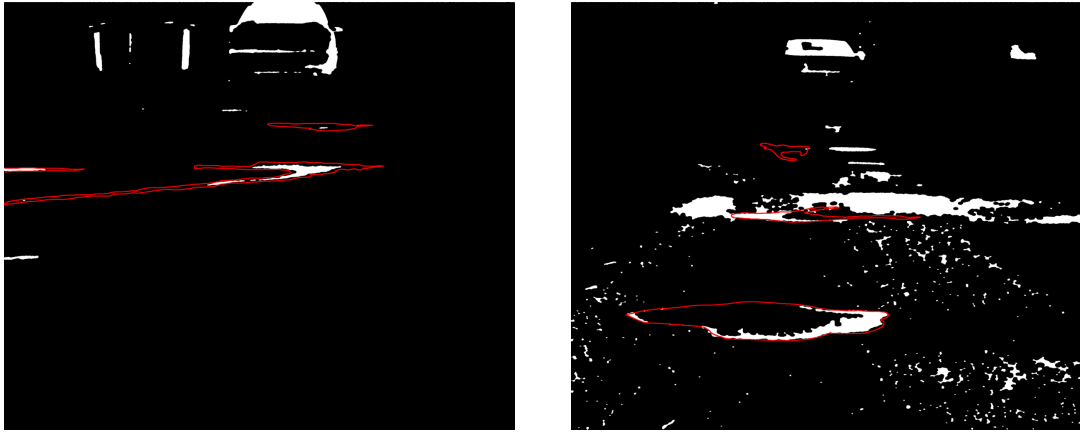
Figure 3.10: The DOP images from Figure 3.9 after applying a threshold and noise-reducing post-processing.

Next, morphological transformations are applied to the image. Since this topic is quite complex by itself, we recommend further reading, if interested, see [KP12]. The transformations result in clearer edges and less noise, which is beneficial for further processing. Note that small true positive water areas are also removed in this process, since their area is not enough to fulfill the not-noise requirement.

3.4.2 Segmentation Based on the Angle of Polarization

In addition to the DOP, we can also use the AOP as a cue for segmentation. So first, the AOP of the original images needs to be calculated. The result can be seen in Figure 3.11
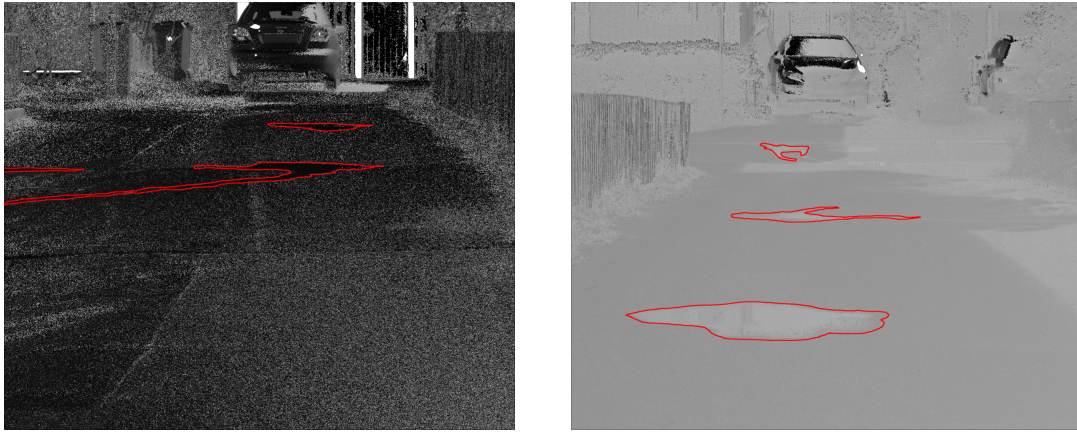
Figure 3.11: AOP false colour images for the water detection algorithm. Water hazards are marked in red. Otherwise, the 8-bit pixel value correlates directly with the AOP.

One can see that the AOP for the water hazards is generally closer to 0° than the one of the surrounding area. Note that while the two values at the water surfaces look different in either picture, it is because 175° is as close to 0° as 5° is. This also explains the supposed noisy nature of the first image.

With the AOP images in place, we can now apply a threshold, as before. The results of that, as well as additional pre-and post-processing can be seen in Figure 3.12.

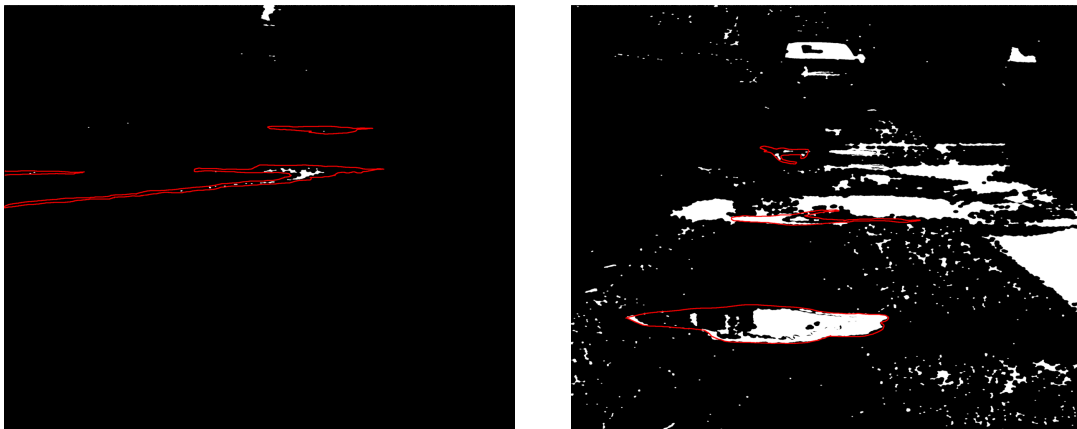**Figure 3.12:** The DOP images from Figure 3.9 after applying a threshold and noise-reducing post-processing.

Note that this is not a general threshold application, where every value above a the threshold is considered a true value, and the other ones as false. In this custom threshold application, we consider all values around the threshold in a certain margin

as a truth value. This is necessary due to the previously mentioned nature of the angles, where $180° = 0°$.

3.4.3 Combining the Information

After applying the thresholds for both the DOP and the AOP, two different binary images are available. From here, two approaches based on two different requirements can be taken. First, the images can be combined via a conjunction. That means that the final image will be true only where both of the original images were true as well. This is particularly useful if one deems false positives worse than false negatives. The system will detect less water hazards in general, but will be more confident.

The second option is to use a disjunction. Here, the final image will be true where either of the original images were true as well. In this case, false negatives are deemed worse than false positives. Here, the system will detect water more frequently, with a lower confidence.

Here, the second approach will be taken. In the use case of an autonomous vehicle driving along a road, we assume that it is less problematic for the vehicle to detect a water hazard incorrectly compared to it not detecting the hazard at all. The combined images can be seen in Figure 3.13.
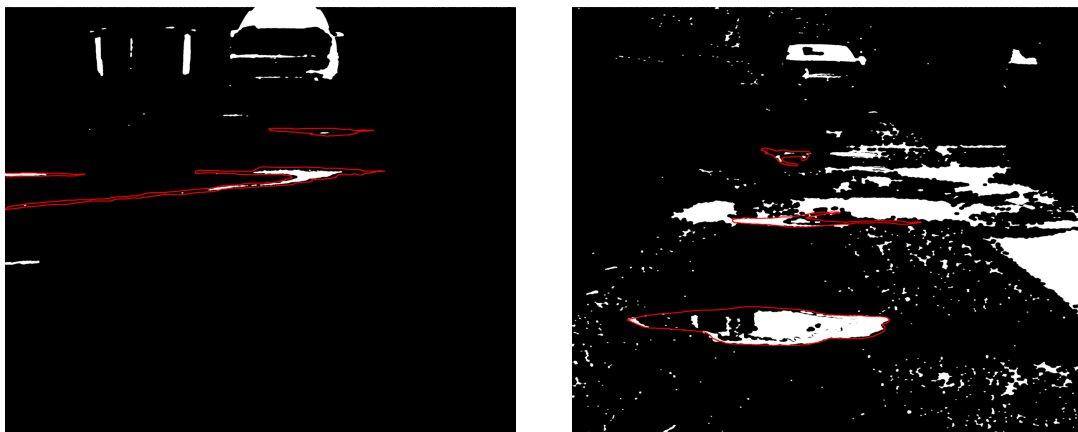
Figure 3.13: Combined binary images from Figures 3.12 and 3.10. Water hazards are marked in red.

In order to track and measure the distance to each individual hazard rather than a general value, a contour algorithm is used. As the name suggests, it provides the coordinates of the contour of the particular segment. In Figure 3.14 you can see the result of applying the contour algorithm to the previous images. Additionally, contours below a certain area size have been removed, in order to further reduce noise.

Each individual contour has been colored differently for demonstration purposes. Now, supposedly knowing each individual hazard, we can apply stereo matching and calculate the distance to the point.
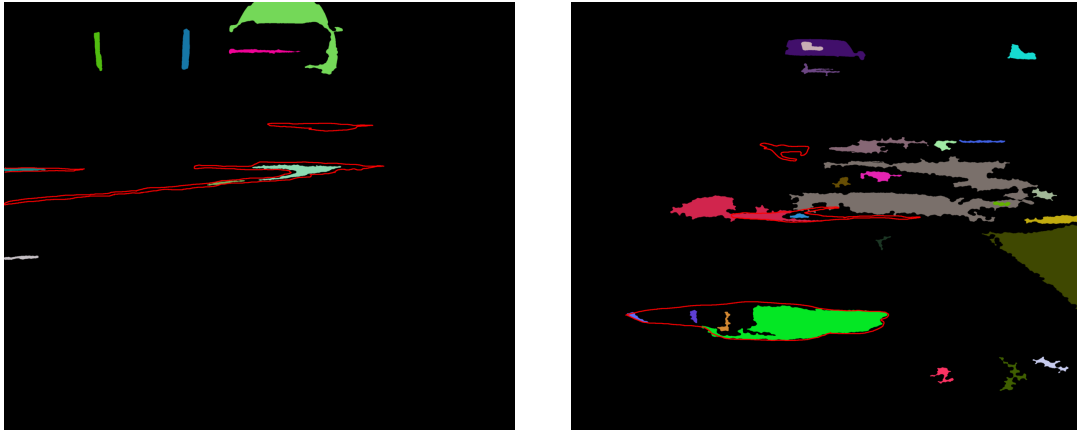
Figure 3.14: Figure 3.13 after applying a contouring algorithm. Individual contours have been colored randomly.

3.4.4 Measuring Distance

Now knowing where the water hazard candidates are, we can use the previously mentioned stereo matching in order to compute the distance from the camera to the given point. We use the original left and right images as provided by the two cameras. They are undistorted using the previously established parameters and then passed to the stereo matching algorithm. Figure 3.15 shows the results of said algorithm, with pixel disparity being encoded in intensity.

Figure 3.15: The filtered disparity maps for Figure 3.8. A brighter value encodes a higher pixel disparity.

4

Results

This section aims to show the results of evaluating the individual components presented in Chapter 3 and thus the accuracy of the IMX250MZR.

4.1 Angle of Polarization

In order to evaluate whether the angle of polarization is measured and calculated properly, the ground truth needs to be established.
For this, we need to establish an accurate source of linearly polarized light. This can be achieved by projecting unpolarized light through a linearly polarized filter. For our purposes, we use linearly polarized foil. The particular set of foil used offers a polarization efficiency of 99.9% [3Dl20].
We can then emulate different angles of polarization by rotating the foil in front of the light source. The camera is kept stationary so the reference frame does not change. The entire setup can be seen in Figure 4.1.
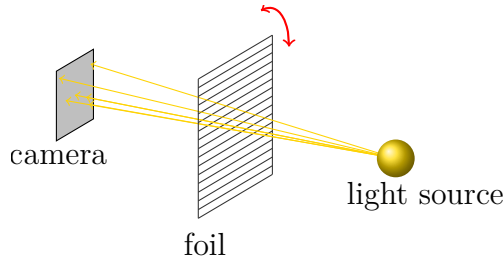
Figure 4.1: Test setup for measuring the Angle of Polarization. The foil is rotated and polarizes the light that is emitted by the light source.

The results of the measurements can be seen in Table 4.1.

One can see that the calculated angles seem to be a little bit higher than the actual angle, with the two biggest outliers being at 90° and 135° actual angle. However, even with those two outliers, the precision of the AOP calculation is high, with an average error of 0.492°. Note that the emitted angles likely are not exactly as stated here, due to manufacturing issues and the manual calibration of the setup itself. However, even a larger error would not cause a big problem for the AOP part of the algorithm either, since the thresholds were determined empirically in the first place.

Table 4.1: Comparison of the actual angle of polarization with the calculated angle, as per setup in Figure 4.1.

actual angle (°)	calculated angle (°)	abs. error (°)
0	0.279	0.279
15	15.025	0.025
30	30.281	0.281
45	45.078	0.078
60	60.329	0.329
75	75.445	0.445
90	90.967	0.967
105	105.554	0.554
120	120.421	0.421
135	136.213	1.213
150	150.588	0.588
165	165.724	0.724
	average error:	0.492

4.2 Degree of Polarization

The calculation of the DOP depends on the differences between the four phases that are used. That means that the calculated DOP is not only going to depend on the actual degree of polarized light, but also on the angle.

In order to examine how the AOP actually affects the DOP, we can reuse the setup from the previous experiment, see Figure 4.1. The specific values can be seen in Table A.1.
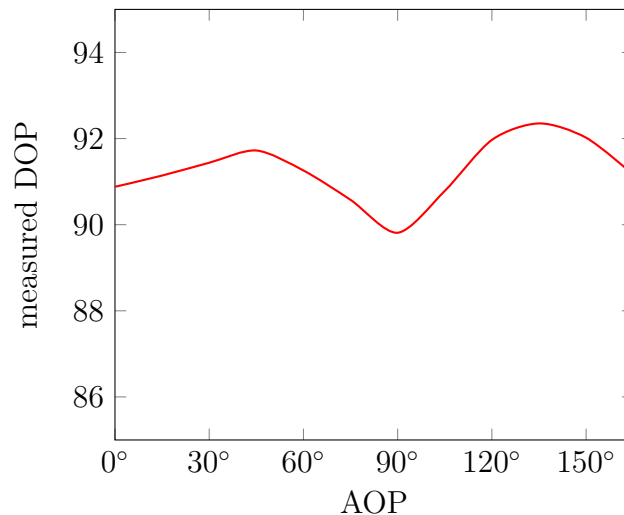
Figure 4.2: measured DOP depending on emitted AOP, based on the setup in Figure 4.1.

The results from the experiment validate the previous claim: The measured DOP fluctuates, depending on the AOP. While the DOP should be 99.9% in theory, we

only reach 92% in this experiment. This could also be due to environmental lighting conditions, where a higher DOP might be present than expected, which in turn will reduce the DOP after passing through the foil, depending on the orientation.

Previous research has also found that the diagonal polarizers on the IMX250MZR have a smaller difference between min- and max value (I_{min}, I_{max}) than their horizontal/vertical counterparts [RRN19]. However, the results here indicate otherwise. At 45° and 135° incoming angle, the diagonal polarizers are at I_{min} and I_{max}, respectively, the other polarizer pair at $\frac{I_{min}+I_{max}}{2}$.

In that case, the difference between I_{max} and I_{min} of the diagonal polarizers determines the DOP. A larger contrast equals a larger DOP, see Equation 3.3. According to the results here, the larger contrast is therefore present on the diagonal polarizers, not the horizontal/vertical ones. This is visible by the clear peaks of the DOP at 45 and 135°.

However, Rebhan, Rosenberger, and Notni used a pre-production model of the IMX250MZR and only exposed the sensor to a specific wavelength. This means that either the characteristics of the sensor changed since then or that the sensor behaves differently at a larger spectrum of wavelengths.

In any case, these values do not cause an issue for the water detection, since the threshold are established empirically, as previously mentioned.

4.3 Distance Measurement

The accuracy of the distance measurement via stereoscopic imaging can be established by taking images, calculating the distance to a given target and then comparing said distance with a manually established one.

Another metric that is to be considered is the reprojection error. It states how well the intrinsic and extrinsic camera parameters like focal length and baseline between the cameras have been calibrated. We can compare the real world values to the calculated ones to see whether the calibration generally worked. It is still favourable to actually calculate those values rather than entering them manually, since they are of generally higher accuracy than manually made measurements.

Table 4.2 shows the real world values compared to the ones established by the calibration. The focal length has been taken from the manufacturer, see [VS 13]. Note that this value might differ slightly due to issues during the production of the lens.

Table 4.2: Comparison between calculated and real world values for baseline and focal length after calibration.

	baseline	focal length
calculated	51.21 cm	35.45 mm
real world	51.2 cm	35.1 mm

We can see that the values do not align perfectly, but are reasonably close to each other. Taking a look at the previously mentioned reprojection error, we reach a good value of 0.335. This means that the necessary intrinsic and extrinsic parameters have been setup well. In order to calculate the distance, we also need the pixel

Figure 4.3: The left input image used for the disparity estimation in Figure 4.4

Figure 4.4: The filtered disparity map for Figure 4.3. A brighter value indicates a higher disparity value.

disparity value, which is established via stereo matching.

Recalling from earlier in Section 2.2, stereo matching works by comparing the pixel values in the left and right image and then returning the distance in pixel between pixels of similar intensity. To know which pixel actually corresponds which, a textured environment is favourable. Having more distinct pixels enables the matcher to more precisely tell which pixels belong together and thus results in a more detailed and accurate disparity map.

We can see this behaviour in Figures 4.3 and 4.4.

The areas in the back contain more distinct features and have more texture than the asphalt in the front. This results in a uniform, and thus bad, disparity map for the the asphalt, whereas the car in the back can clearly be distinguished from the rest.

Ignoring this fact and just taking a look at the performance of the stereo matcher on a high-feature area such as the car in the back, we can see that the calculation actually works pretty well. Applying the previously established baseline, focal length and now the pixel disparity to Equation 2.19, we can calculate a distance of 32.7m from the camera to the back of the car. This estimated distance is very close to the actual real world distance of ca. 33.2m. The small difference shows that the distance estimation and the stereo matching are working properly, if supplied with enough features.

5

Discussion

This chapter discusses the results of the algorithm and methods presented in Chapter 3. Both example images produced quite different, thus inconclusive, results, which makes an investigation into the causes necessary.

5.1 Setup

In order to investigate and explain the results of the example images as shown in the previous section, a dataset of images was established. `image_1` and `image_2` are part of said dataset.

For this, four different values for ψ_o were used, based on the available environment. Then, images were taken at these angles at three different times of day (10:00, 14:00 and 18:00 CEST) in order to produce different solar azimuths. This resulted in a total of 12 images, each with a distinct ψ_r. The specific values can be seen in Table A.2. In order to analyze the water detection, we will categorize the possible surface conditions as in Table 5.1

Table 5.1: Surface condition categories.

is water	category	description
true	wet road	A piece of wet road, without a puddle
	puddle (sky)	A puddle reflecting the sky
	puddle (non-sky)	A puddle not reflecting the sky
false	obstacle	Any reflective non-water surface
	shadow	Non-wet road in the shadow
	road	Non-wet road not in the shadow

For each image, the DOP and AOP values have been manually extracted, as an average of multiple positions in the scene.

5.2 Degree of Polarization

The previous experiments showed that the DOP can be used as a cue for segmentation. However, in the case of `image_2`, applying the threshold produced mixed results. Parts of the water surface were below the threshold, whereas parts of the

asphalt were above it. Additionally, shadows proved to result in different DOP values than the surrounding background.

5.2.1 Differences in Water Surfaces

First, we will compare the different water surfaces in order to analyze why certain parts of the water surfaces were below the threshold, see Figure 5.1.
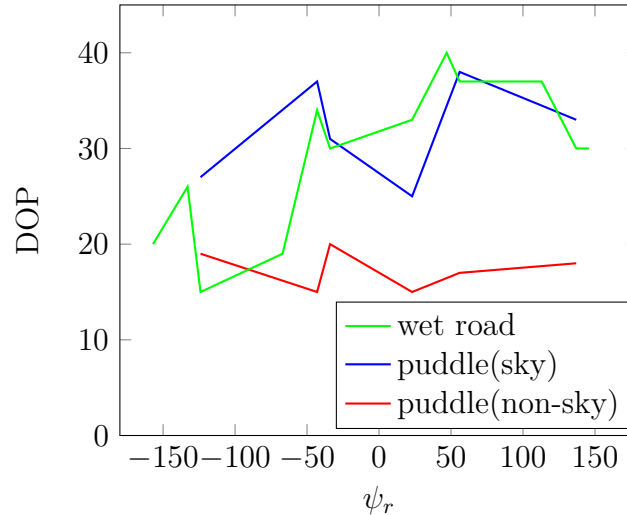

Figure 5.1: The DOP of the three different water categories at a given ψ_r.

The graph shows that puddle (non-sky), generally speaking, provides the lowest value out of the three. The value does not seem to change much depending on ψ_s neither. Since there is no direct impact by the light from the sky, it shouldn't have a huge impact either. This is in accordance with previous research, which came to the conclusion that water is less polarized if it does not reflect the sky [Bin+07].

In the case of puddle (sky), we can see that the DOP roughly follows the sky polarization pattern. There, the DOP is highest at $\pm90°$ from the sun, which can be observed here as well. The pattern is also symmetrical along the solar meridian. The DOP value for wet asphalt changes quite drastically depending on the relative angle. With a positive ψ_r, the DOP is notably higher compared to the negative counterpart. This suggests that the DOP on a rough surface such as asphalt is more dependent on the AOP in the sky compared to the reflective counterparts. While the sky DOP is mirrored along the solar meridian, the AOP is not. However, the DOP is generally still higher than the one for puddle (non-sky).

This does partially explain why on `image_2`, the puddle in the foreground is only detected in the front part, where the road is wet. In the particular image, the DOP value for both types of puddle is lower than the one for wet road.

5.2.2 Differences Between Water and Non-Water

Besides the missing detection of the some water surfaces in `image_2`, a lot of the road is detected as well. In order to investigate this, we will have to compare the

DOP of the road with the one for the water categories. This can be achieved by calculating the contrast between the values.

A low contrast indicates a smaller difference between the value, thus a smaller window for a threshold value to properly segment both categories from each other. This also suggests worse detection quality, caused again by the window for the threshold. Contrast is calculated as in Equation 5.1 [Mic27].

$$c = \frac{I_{max} - I_{min}}{I_{max} + I_{min}} \tag{5.1}$$

For this, the wet asphalt and puddle (sky) have been merged into a single category. Puddle (non-sky) will not be considered here, since its DOP proved to be too low to be usable. The calculated contrast can be seen in Figure 5.2.
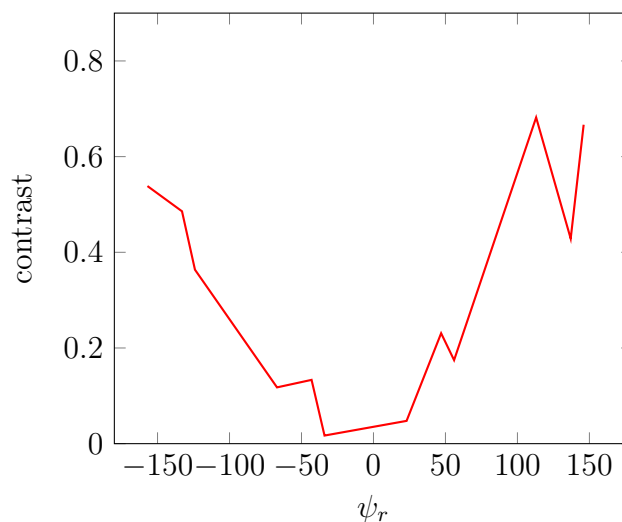
Figure 5.2: The contrast between the DOP of the road and the average DOP of puddle(sky) and wet road.

As the the results from `image_1` and `image_2` showed, the quality of detection was lowest when facing the sun. This correlates with a low ψ_r, which also has the lowest contrast value. One can see that the contrast is lowest with a low ψ_r. This does support the previous observation. We can also still see the higher contrast is higher with positive ψ_r.

Taking a closer look at just the non-water data in Figure 5.3, we can see that the DOP value for the road is higher with a lower ψ_r. While this follows the same pattern as the DOP for the water data, the DOP is much lower when facing away from the sun, therefore increasing the contrast and improving detection.

Figure 5.3: The DOP of the three different non-water categories at a given ψ_r.

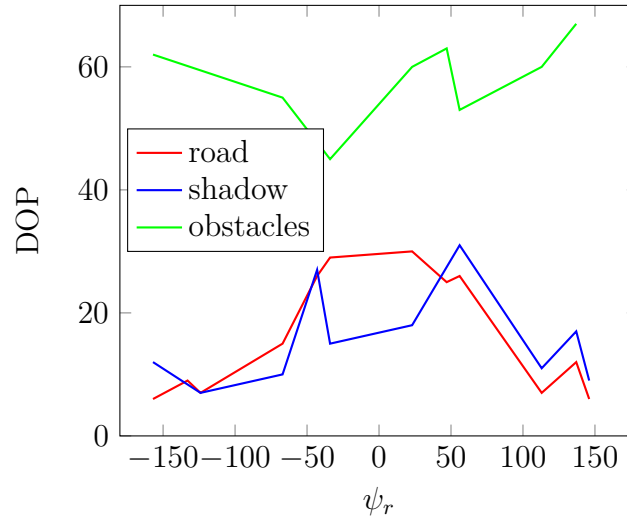The graph also shows that the value for the shadow follows the sky polarization pattern, being highest at $\pm 90°$ away from the sun. This is similar to the pattern of puddle (non-sky), where the impacting light is also highly unpolarized. Due to the rough nature of the road surface, it reflects more area in the sky, which likely results in the observed pattern. The values from the road and the shadow are relatively close though, the only difference being when the camera is facing the sun.

As for the road value, it is unclear what causes the peak at $\psi_r = 0°$.

The value for general obstacles, just as car windows or letterboxes is extremely high. In fact, it is much higher than even the highest DOP for water surfaces. So in order to inhibit the detection of those obstacles, an additional inverted threshold will need to be applied to the DOP image. Since the DOP values for the obstacles are so high, there is little chance to mistakenly remove actual water surfaces from the image. It has to be noted that the values for the obstacle are taken from different surfaces, the values therefore only provides a general suggestion and not a conclusive statement

It has to be noted that all of the values used for these graphs are only mean of multiple locations within the image itself. There are vast differences in DOP, especially when it comes to different types of asphalt. In just a single image, the DOP of the road ranges from 22% up to 45.3%, for example. This inhibits choosing a proper threshold as well.

5.3 Angle of Polarization

Similar to the DOP, previous experiments have shown that the difference in AOP of a water surface compared to the surrounding asphalt is high enough for segmentation, mostly when 90° away from the sun.

The difference in AOP of the different water surfaces was negligible. They will therefore be combined into a single category. Additionally, the values for obstacles were very different from the rest of the scene and will therefore be omitted here as well.

Taking a closer look at `image_2`, we can see that the detected regions are the actual water surface and partially road in shadow. We can investigate this behaviour by comparing the different AOP values, see Figure 5.4. Here, we will again be referring to the interval of $[-90, 90]$ for the AOP for a more intuitive visualization.
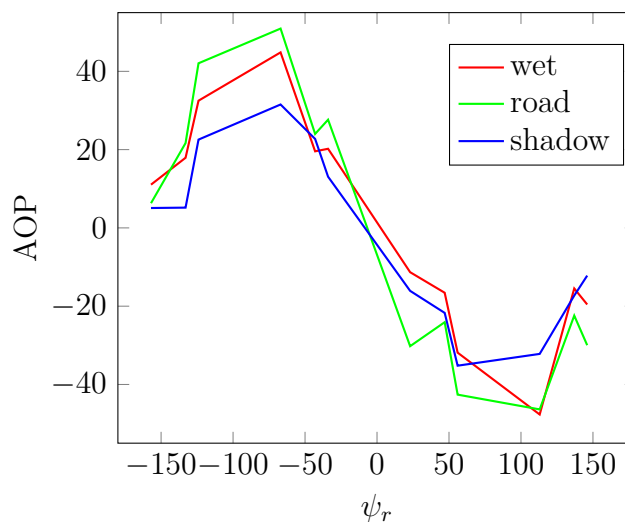

Figure 5.4: The AOP of the water, shadow and road at a given ψ_r.

The graph shows that the largest deviations from $0°$ are when facing $90°$ away from the sun. This is also the same pattern as previously observed during the experiments in Section 3.3. Comparing the AOP values on the ground with the ones in the sky shows that a positive AOP in sky results in a negative value on the ground, and vice versa.

Surprisingly, the AOP for shadow appears to be closer to $0°$ than the AOP for water. This might be attributed to the fact that there is no direct sunlight, which increases the amount of incoming unpolarized light. The highly unpolarized light therefore appears to cause a lower AOP than the more polarized counterpart. In areas with a high DOP in the sky, $\pm 90°$ from the sun, the AOP is higher as well. The the closer the DOP gets to 0, so does the AOP on the ground. This applies to the wet surfaces as well. While the reflection is more pronounced due to the specular nature of the surface compared to the shadow, the larger amount of polarized light still amounts in a larger AOP value.

Taking a closer look at the AOP of the road, it seems like the value is offset by $90°$ from the sky polarization pattern, see Figure 5.5. This means that an sky AOP of $60°$ results in a surface value of $-30°$ and so on. This is probably caused by the reflection itself, but could not be verified.
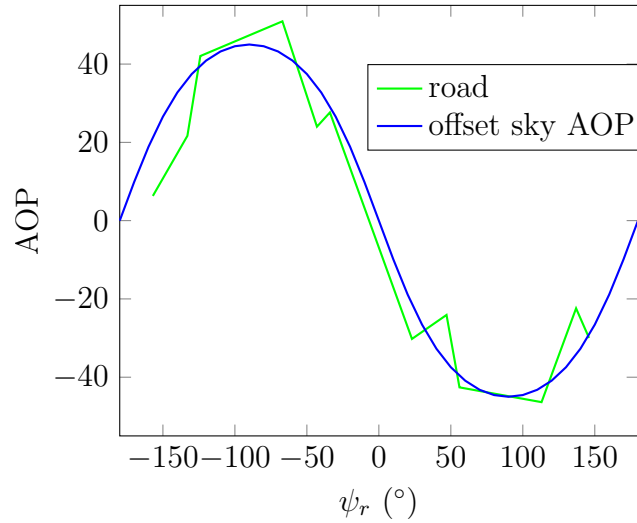
Figure 5.5: Comparison between the AOP for road and the AOP of the sky, offset by 90°.

Figure 5.6 shows the contrast between the AOP of the road and the AOP of a water surface.
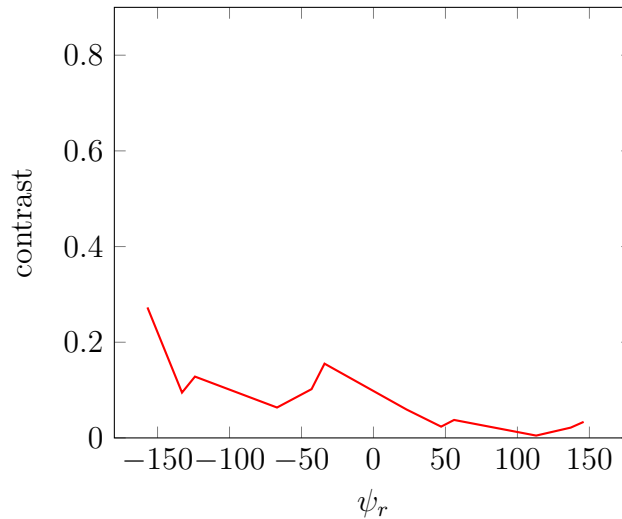
Figure 5.6: The contrast between the AOP of the road and the average AOP of a water surface.

The contrast is overall really low, which explains the mixed results in `image_2`. The highest contrast appears at $\psi_r = -157$, which explains the good detection in `image_1`. The generally very low contrast seems to indicate the AOP is a worse metric than the DOP. However, the deviation of values within the same category is much lower compared to the DOP. Where the DOP would deviate from 22% up to 45.3% on the road, as previously mentioned, the AOP in the same image only deviates from 7.3° to 13° in the same category. The lower variance should allow for a more robust threshold.

5.4 Contoured Areas

After applying the contouring algorithm, each individual hazard should be identified. Ignoring the obstacles in `image_1`, this worked really well and provided the outlines of two out of the three hazards. The shape of the contour followed the ground truth reasonably well. Only smaller sections of the water hazard were ignored, due to the kernel size during the morphological transformations. This is also likely the cause for ignoring the third puddle. In the DOP image, see Figure 3.9, is is clearly visible. Only after applying the threshold and the morphological transformations, it disappears.

On the other hand, in `image_2`, a lot of false positive detections are present. While 2 out of the 3 areas have at least some form of detected segment within them, the general shape does not fit the ground truth. This, combined with the amount of false positives makes the results for this image unusable.

5.5 Distance Measurement

The results from the stereo matching step proved to be unsatisfying for when it comes to the actual road surface. As already mentioned in Section 4.3, this is likely due to the low amount of distinct features on the asphalt.

This is caused by the distance from the camera to the road surface itself, thus making the actual features appear smaller and less clear. This effect is increased in areas that are not in focus of the camera, thus resulting in an even smoother looking road surface.

One way to combat this is to not rely on the original image itself, but rather take the final mask of the water detection algorithm as input. This is favourable since we only want to measure the distance to these points anyways. Since the mask is a binary image it has very clear edges, which are beneficial to the stereo matching step. However, being able to use this binary image also requires both masks from the left and right image to be identical or very similar at least. If the outline of the water hazard on either camera differs greatly from the other one, then no proper matching can take place.

This approach to stereo matching was implemented, but also produced unsatisfactory results, due to the poor nature of the detected themselves, as has been seen previously.

5.6 Additional Remarks

Most of the algorithm and explanations in the previous sections have only relied on a small amount of parameters. Only the azimuth of the sun and the observer have been taken into account when it comes to environmental parameters. These are only a fraction of the large parameter space that is the lighting in an outdoor scene.

For example, the surface of a puddle is not perfectly flat but influenced by wind or vibrations on the ground. This impacts reflection and therefore the AOP and

DOP values. In terms of reflection, the internal reflection within a puddle and the resulting change in polarization has not been discussed neither. Additionally, all of the data that has been collected and evaluated throughout the run of this thesis has purposefully been taken only during clear skies.

Most of these omissions and decisions have been taken in an effort to reduce complexity, some simply due to missing environmental data. For example, knowing the geometry of the road would enable the estimation of incidence angles. An additional factor for the road is the type of asphalt. For example, freshly laid asphalt appears to be more reflective than older asphalt, which could impede detection rates as well. It could also be possible to remove vegetation at the side of the road by deploying the previously mentioned similarity degree. Since there were no occurrences of false positives due to the vegetation, this will likely not result in better detection rates.

There are more possibilities in order to increase the amount of data that is available to the system, which in turn could increase the detection quality. However, each increase in data results in an increase in complexity as well. Gathering this data can be both labour and cost intensive as well.

This increase in information does not change that fact that the contrast in both DOP and AOP between water and non-water surfaces remains low when facing the sun. This might not be the case when the sky is overcast though. This would partially eliminate the sky polarization and thus remove some of the implications of reflecting polarized light, as previously discussed.

An additional way to combat the effect of sky polarization would be to rely on a distributed system. In the case of two vehicles driving towards each other, one could detect water reliably. Sharing that information between the vehicles could result in a more robust system.

More sensors are likely not able to overcome the issues with polarization when facing the sun. They have to be used and evaluated independently of the polarization in order to improve detection rates.

General improvements to the detection quality could be gained by relying more on general image processing. For example, a partial shadow could likely be excluded by ignoring areas below a certain general intensity value. Also, the non-polarization based approaches as shown in Section 1.1 could be combined with the polarization data that has been gathered and produce a more robust system.

Nevertheless, the issues in detection arise from the environment itself and not the IMX250MZR. As the evaluation has shown, the polarization data is captured relatively precisely. Having four differently aligned polarizing filters within the same camera rather than multiple cameras with external filters also enables a more robust stereo matching. The pixel values in either camera should be the same, whereas they are not in the other setup, by design.

The time in order to compute one set of pictures is relatively high. It takes around four seconds for a pair of images to be processed in terms of polarization and also applying the stereo matching step. This could be improved greatly by removing the stereo matching step, which has been found to be working poorly. As a consequence of the removal, the resolution of the images can also be reduced. The main argument for a high resolution was the better precision for the stereo matching at longer distances. With this out of the way, a lower resolution results in less pixels to be

considered and therefore faster computation overall. The calculation is also done on a CPU, with little parallelization. Moving parts of the calculation to a dedicated GPU as well as optimizing the code in general could reduce the time further.

A comparison against previous approaches has been omitted due to the poor detection quality when facing the sun. It was never to the goal to produce a reliable system which would work better than previous ones, but rather only rely on the polarization cues that the IMX250MZR provides.

6
Conclusion

In this thesis, the detection of water hazards by deploying a dedicated polarization image sensor was investigated in an urban environment.

The accuracy or the IMX250MZR has been evaluated in terms of AOP and DOP. Comparing the measured value with the emitted AOP showed a low average error of $0.492°$. The comparison of the DOP values showed that there is a small difference in transmittance ratio between the horizontal/vertical and diagonal filters, confirming the results of previous work in this area. The DOP values were close to the supposed real world values, yet a bit lower, which is likely attributed to the previously mentioned transmittance ratios. These two factors combined state that the data coming from the IMX250MZR is quite accurate and can be used to measure polarization precisely.

Additional experiments in regard to the influence of the sun on the polarization on the ground were conducted. Depending on the ψ_r, the polarization on the ground differed greatly, as was to be expected in accordance to the Rayleigh sky model. The experiments were conducted in an controlled environment, which allowed to calculate the theoretical DOP value on the ground. While the experimental values were in line with the theoretical ones, they were lower than expected. This is likely caused by the simplified environmental model that was used, making an accurate prediction not possible.

Using the IMX250MZR in a stereo setup proved to be difficult. This is not caused by the sensor itself, but rather the urban environment. The stereo matching step provided poor results, due to the low amount of features on the asphalt. More highly textured regions provided accurate disparity and thus distance measurement results. This made measuring the distance to detected water hazard on the road surface unfeasible with the current stereo matching algorithm.

The quality of detecting said water hazard depends greatly on ψ_r. This dependency has been identified as being the contrast between water and non-water surface values. A high contrast enables a more accurate threshold for separating water and non-water. Low contrast values were generally found when facing the sun, high values when facing away. This means that segmenting water hazard via image processing does provide promising results, but only when the camera is facing away from the sun. However, the poor detection quality when facing the sun results in an overall unreliable system.

The urban environment provided additional challenges compared to an outdoor environment. The presence of shadows and man-made reflective surfaces made the distinction between water and non-water more difficult, due to the difference in po-

larization. Also, as previously mentioned, the relatively smooth asphalt proved to be a large obstacle for the stereo matching algorithm.

In conclusion, the IMX250MZR is an accurate source of polarization data. However, a more precise model of the environment in terms of polarization is necessary in order to be able to accurately segment water hazards from non-water surfaces, when solely relying on image processing. More sophisticated approaches in terms of stereo matching might also allow for the accurate measurement of distances on the road surface.

Bibliography

[3Dl20]   3Dlens Corporation. *Linear Polarizer Film.* 2020. URL: `https://3dlens.com/linear-polarizer-film.php`.

[Bag09]   Greg Baguley. *Stereo Tracking of Objects with respect to a Ground Plane.* University of Canterbury, 2009.

[Bin+07]   Bin Xie et al. "Polarization-based water hazards detection for autonomous off-road navigation". In: *2007 IEEE/RSJ International Conference on Intelligent Robots and Systems.* 2007, pp. 3186–3190. DOI: `10.1109/IROS.2007.4398994`.

[Bra00]   Gary Bradski. "The OpenCV Library". In: *Dr. Dobb's Journal of Software Tools* (2000).

[BW13]   Max Born and Emil Wolf. *Principles of optics: electromagnetic theory of propagation, interference and diffraction of light.* Elsevier, 2013.

[Gol16]   Dennis H. Goldstein. *Polarized light.* CRC press, 2016.

[Han+18]   Xiaofeng Han et al. "Single Image Water Hazard Detection using FCN with Reflection Attention Units". In: *The European Conference on Computer Vision (ECCV).* 2018.

[Hec13]   Eugene Hecht. *Optics: Pearson New International Edition:* Pearson Education M.U.A., Aug. 2013. ISBN: 9781292034805.

[HI16]   Rostam Affendi Hamzah and Haidi Ibrahim. "Literature survey on stereo vision disparity map algorithms". In: *Journal of Sensors* 2016 (2016).

[HMD14]   Joop W. Hovenier, Cornelis Van der Mee, and Helmut Domke. *Transfer of polarized light in planetary atmospheres: basic concepts and practical methods.* Vol. 318. Springer Science & Business Media, 2014.

[HZ03]   Richard Hartley and Andrew Zisserman. *Multiple view geometry in computer vision.* Cambridge university press, 2003.

[KP12]   Sreedhar Reddy Kollem and B. Panlal. "Enhancement of Images using Morphological Transformation". In: *CoRR* abs/1203.2514 (2012). arXiv: `1203.2514`. URL: `http://arxiv.org/abs/1203.2514`.

[Li+14]   Li Li et al. "A method to calculate Stokes parameters and angle of polarization of skylight from polarized CIMEL sun/sky radiometers". In: *Journal of Quantitative Spectroscopy and Radiative Transfer* 149 (2014), pp. 334–346.

[LLP96]   J. Lehner, U. Leonhardt, and H. Paul. "Unpolarized light: Classical and quantum states". In: *Phys. Rev. A* 53 (4 Apr. 1996), pp. 2727–2735. DOI: `10.1103/PhysRevA.53.2727`. URL: `https://link.aps.org/doi/10.1103/PhysRevA.53.2727`.

[LS11]   Sang Hwa Lee and Siddarth Sharma. "Real-time disparity estimation algorithm for stereo camera systems". In: *IEEE Transactions on Consumer Electronics* 57.3 (Aug. 2011), pp. 1018–1026. ISSN: 1558-4127. DOI: 10.1109/TCE.2011.6018850.

[Mee91]   Jean Meeus. *Astronomical Algorithms*. Willmann-Bell, Incorporated, 1991. ISBN: 0943396352.

[Mic27]   Albert Michelson. *Studies in Optics*. University of Chicago Press, 1927.

[MMK13]   Manaf Mahammed, Amera Melhum, and Faris Kochery. "Object distance measurement by stereo vision". In: *International Journal of Science and Applied Information Technology (IJSAIT)* 2.2 (2013), pp. 05–08.

[MV08]   Jernej Mrovlje and Damir Vrancic. "Distance measuring based on stereoscopic pictures". In: *9th international PhD workshop on systems and control: young generation viewpoint*. Vol. 2. 2008, pp. 1–6.

[NMM17]   Chuong V. Nguyen, Michael Milford, and Robert E. Mahony. "3D tracking of water hazards with polarized stereo cameras". In: *CoRR* abs/1701.04175 (2017). arXiv: 1701.04175. URL: http://arxiv.org/abs/1701.04175.

[RMB11]   Arturo Rankin, Larry Matthies, and Paolo Bellutta. "Daytime water detection based on sky reflections". In: *2011 IEEE International Conference on Robotics and Automation*. IEEE. 2011, pp. 5329–5336.

[RRN19]   David Rebhan, Maik Rosenberger, and Gunther Notni. "Principle investigations on polarization image sensors". In: *Photonics and Education in Measurement Science 2019*. Vol. 11144. International Society for Optics and Photonics. 2019, 111440A.

[RSC05]   Michael Robinson, Gary Sharp, and Jianmin Chen. *Polarization engineering for LCD projection*. Vol. 4. John Wiley & Sons, 2005.

[Sai+99]   Megumi Saito et al. "Measurement of surface orientations of transparent objects by use of polarization in highlight". In: *JOSA A* 16.9 (1999), pp. 2286–2293.

[San65]   Oscar Sandus. "A Review of Emission Polarization". In: *Appl. Opt.* 4.12 (Dec. 1965), pp. 1634–1642. DOI: 10.1364/AO.4.001634. URL: http://ao.osa.org/abstract.cfm?URI=ao-4-12-1634.

[She+17]   Jie Shen et al. "Polarization and solar altitude correlation analysis and application in object detection". In: *2017 International Conference on Progress in Informatics and Computing (PIC)*. Dec. 2017, pp. 179–183. DOI: 10.1109/PIC.2017.8359538.

[SM07]   Joseph Shapira and Samuel Miller. *CDMA radio with repeaters*. Springer Science & Business Media, 2007.

[Son18]   Sony Semiconductor Solutions. *Polarization Image Sensor with Four-Directional on-chip Polarizer and global shutter function*. 2018. URL: https://www.sony-semicon.co.jp/e/products/IS/polarization/technology.html.

[Sze10]   Richard Szeliski. *Computer vision: algorithms and applications*. Springer Science & Business Media, 2010.

[SZL15]   Haiyan Shao, Zhenhai Zhang, and Kejie Li. "Research on water hazard detection based on line structured light sensor for long-distance all day".

In: *2015 IEEE International Conference on Mechatronics and Automation (ICMA)*. IEEE. 2015, pp. 1785–1789.

[VS 13]   VS Technology Corporation. *VS-3514H1 Spec Sheet.* 2013. URL: https://www.rmaelectronics.com/content/VST%20America/VS-H1%20Series/35mm/VS-3514H1_SpecSheet_E.pdf.

[Wan+14]   Yujie Wang et al. "Design of a device for sky light polarization measurements". In: *Sensors* 14.8 (2014), pp. 14916–14931.

[Yan+17]   Kailun Yang et al. "Detecting traversable area and water hazards for the visually impaired with a pRGB-D sensor". In: *Sensors* 17.8 (2017), p. 1890.

[YK03]   X. J. Yu and H. S. Kwok. "Optical wire-grid polarizers at oblique angles of incidence". In: *Journal of applied physics* 93.8 (2003), pp. 4407–4412.

[YXL09]   Tuo-zhong Yao, Zhi-yu Xiang, and Ji-lin Liu. "Robust water hazard detection for autonomous off-road navigation". In: *Journal of Zhejiang University-SCIENCE A* 10.6 (2009), pp. 786–793.

[Zha+13]   Yibing Zhao et al. "Research of water hazard detection based on color and texture features". In: *Sensors & Transducers* 157.10 (2013), p. 428.

[Zho+17]   Guanhua Zhou et al. "Polarization patterns of transmitted celestial light under wavy water surfaces". In: *Remote Sensing* 9.4 (2017), p. 324.

Bibliography

A
Appendices

Table A.1: Comparison of the actual angle of polarization with the calculated angle, as per setup in Figure 4.1.

AOP (°)	measured DOP (%)
0	90.880
15	91.141
30	91.439
45	91.723
60	91.259
75	90.577
90	89.813
105	90.785
120	91.969
135	92.352
150	92.020
165	91.163
mean:	91.260
standard deviation:	0.705

Table A.2: Combination of observer and solar azimuth angles for the investigation of DOP and AOP.

ψ_o (°)	ψ_s (°)	ψ_r (°)
62	118	56
62	197	135
62	269	-153
152	120	-32
152	199	47
152	269	117
242	117	-125
242	196	-46
242	269	27
332	119	147
332	198	-134
332	269	-63